Facultad de Ciencias, Universidad de Zaragoza

Departamento de Física de la Materia Condensada

Trabajo de Fin de Máster

Propiedades topológicas en nanofotónica: materiales de anchura atómica en presencia de nanoestrcturas metálicas

Fernando Lorén Mastral

Julio de 2020

Supervisado por:
Luis Martín Moreno

Faculty of Science, University of Zaragoza

Department of Condensed Matter Physics

Final Master's Thesis

Topological properties in nanophotonics: atomic-width materials in the presence of metallic nanostructures

Fernando Lorén Mastral

July 2020

Supervised by:
Luis Martín Moreno

"Science knows no country, because knowledge belongs to humanity, and is the torch which illuminates the world. Science is the highest personification of the nation because that nation will remain the first which carries the furthest the works of thought and intelligence."

- Louis Pasteur

I would like to dedicate these lines to thank my family for their endless patience and tireless support in my pursuits. To my friends Juan, Marcos and Mateo, who have been a beacon of passion for physics throughout my academic journey. And to my friend Carlos, who has mostly suffered my ups and downs in this confinement time.

Of course, I must also thank Luis, for he has opened up a new challenging world to me. His unflagging guidance and his immeasurable support have allowed me to grow up in the quest for knowledge.

This Final Master's Thesis is the result of work conducted under the grant *Programa de Iniciación a la Investigación (PI2-ICMA)* awarded by Instituto de Ciencia de Materiales de Aragón (ICMA).

Contents

Introduction

In 2004 the few-layer graphene was electrically studied [1], which granted the Nobel Prize in Physics for its authors (A. K. Geim and K. S. Novoselov) six years later. Since then, the study of two-dimensional (2D) materials has been widely thriving until it became the state-of-the-art science that it is now. Diverse materials such as metals, superconductors, semiconductors or insulators have been acquired in its 2D form. Nowadays, Transition Metal Dichalcogenides (TMDs) are a cutting-edge type of 2D semiconductors, which shines because of its outstanding properties potentially applicable to optics and optoelectronics [2–7].

What we now refer to as Surface Plasmon Polaritons (SPPs) was predicted as a bound electromagnetic (EM) mode at a dielectric-metal interface by R. H. Ritchie [8] in the 1950s. The utmost confinement of these bound modes on the metal surface and its extreme sensitivity to changes at the surface environment open up a broad range of applications such as chemical sensing or bioimaging, amongst others [9]. Over the years, noble metals have positioned themselves as the most promising materials to host plasmons (SPPs) in the optical regime [10].

The study of the EM resonances through metallic nanostructured arrays has been a very active area of research since in 1988 T. W. Ebbesen et al. found out a phenomenon known as Extraordinary Optical Transmission (EOT) [11], which resonantly enhances the transmittance of such periodic arrays of holes through plasmons. Thereafter, a countless number of different designs have been studied [12–14]. EOT is so interesting because of its wide range of applications, such as sensing, spectroscopic devices or colour filters [15].

Since the generalization of the so-called Berry phase was made by M. V. Berry in 1984 [16], topology and physics have been in touch via several areas such as condensed matter physics. One of the main results of this association is the quantum Hall effect, intimately related to the Chern numbers and the Berry phase. In the end, the idea of creating a system with topological discretised indices is protecting it against decoherence or other "destructive" phenomena. Berry phase was also used by K. Y. Bliokh et al. in order to explain the Coriolis effect in optics [20], which is extremely useful to study the spin-orbit coupling effects that arise when a EM wave carrying intrinsic angular momentum interacts with a medium.

So, in this work, we will combine the three elements discussed so far in order to study the emerging phenomena. As a result of this combination we will have a 2D layer placed over a metallic slab with nanoapertures. The 2D material (TMD) will provide us a stratum where light-matter interaction becomes possible via its characteristic spin-orbit coupling. And the drilled metallic nanostructure (noble metal) will be the place where the SPPs will take place. Lastly, topology resides in the origin of the phenomenon which will allow us to break the system symmetry with regard to the handedness of the incident polarization: the geometric phase momentum derived from the topological Berry phase [20] will provide us a spin-momentum locking. This will lead to chirality, for which one potential application would be using a nanophotonic structure where we could control the EM fields in order to make them resonate with chiral molecules, widely used in biology or pharmacology. In fact, this system has been experimentally explored by C. Genet et al. [21] and our labour now is to establish a theoretical framework where their results may rely on. Through the course of this work, we have been in touch with the research group where C. Genet belongs to. This has enabled us to have enlightening talks with them, providing a better approach to the system due to their previous knowledge about it.

Objectives and outline

This Final Master's Thesis has born as a result of intense collaboration with the experimental research group "Laboratoire des Nanostructures" at "Institut de Science et d'Ingénierie Supramoléculaires" (ISIS) at Strasbourg, France. Accordingly, the main objective of this thesis is the development of a theoretical framework from where we can observe the experimental results provided by this world-class research group and presented in [21]. This theoretical model that we have formulated intends to explain qualitatively the key points addressed in [21], as well as to contribute bringing renewed outlook and insight. We will focus on a qualitative approach because of the expensive computational cost that a quantitative refinement would have. However, it is noteworthy that the model we will present could be also used for this refinement.

The physical system that we want to study via this theoretical model is composed by only two elements: an *atomic-width material* in the presence of a *metallic nanostructure*. Therefore, the first secondary objective is the characterisation of both. In Sec. 1 we will discuss the physical features that we need to know about them, such as the atomically thin material conductivity or the metal dielectric constant.

After that, we will present the four different cases of system that we will consider. Furthermore, in Sec. 2.1, although in greater detail in App. A, we will explain the procedure to obtain the governing equations for those four cases, via using the coupled-mode method [14].

Once we will have derived the governing equations, we will have to check the correctness of them. For that purpose, we will consider the simplest possible system and we will compare its results with those presented in [13] and with our intuition (see Sec. 3). Both the simplified governing equations set and its corresponding spectrum will be verified respect [13]. On the other hand, our original governing equations will be more general than others presented in the literature. In fact, this will be the first time that these more generic equations will be derived.

After testing our model, we will be prepared to address the general problem of reproducing the results provided in [21]. However, in order to gain insight on the physical processes in our system, we will approach the experimental setup stepwise, trying to extract useful information from each additional feature implemented in it (see Sec. 4).

In Sec. 4.1 we will consider a standard rectangular holey grating for our metallic nanostructure (akin to [13]) and we will study the main aspects that arise when we consider the absorption of the whole system. Basically, we will focus on the metal and 2D layer absorptions, but also in the production of surface plasmon polaritons (SPPs), which will be treated separately in Sec. 4.2.

And finally, we will introduce in our system the last characteristic to recover the configuration used in [21]: an stepwise rotation of the apertures (dimples) along the unit cell of our metallic nanostructure. We will discuss a new effect that emerges from this rotation: the geometric phase momentum (see Sec. 4.3). The explanation of this new topological effect originates from the Berry phase, as it is described in [20, 21].

Our last objective will be to study the coupling between the 2D layer and the geometric phase plasmon (observed in [21] and presented in Sec. 4.4) and its dependence on five different parameters of the system (see Sec. 4.5). And ultimately, we will propose a novel type of unit cell.

1 Features of our system

Our work will be based on the properties of two main structures: first, a two-dimensional (2D) layer composed of a Transition Metal Dichalcogenide (TMD), whose more interesting aspects will be described later; second, a metallic slab which will be typically chosen as gold and it will be drilled, either by holes or by dimples.

1.1 Absorption spectrum of a WS_2 monolayer

In this section we will intend to give an idea of how interesting TMDs are and why we want to use them for our study. After that, we will consider an specific TMD, tungsten disulfide, which will be used throughout this dissertation, and we will explore it more closely.

Firstly, there are several 2D semiconducting materials which may be attractive, like graphene, phosphorene, TMDs, a combination of them (so-called van der Waals heterostructures, vdWHs), etc. All of them share some qualities but they also differ in some other properties, which opens up a wide range of different potential applications.

Due to the two-dimensionality, charge confinement and reduced dielectric screening are common for them, which entail that the optical properties are dominated by excitonic (electron-hole) effects. Furthermore, their Bohr radius is larger than layer width, which implies that quantum confinement increases the exciton binding energy, changing their absorbing and emitting wavelengths. Both phenomena produce that excitons are bound even at room temperature, making them fruitfully tunable.

That said, the chemical formula for the TMDs is MX_2, where M is a transition metal and X is a chalcogen ($X = S, Se$). In particular, we will discuss the group-IV transition metal dichalcogenides, with $M = Mo, W$. We will use them because, apart from their strong light-matter coupling due to the previous arguments, they also present direct-band gaps in the near-infrared and visible regimes, which is a key feature in order to develop applications in optics and optoelectronics because it enhances the light-matter interaction.

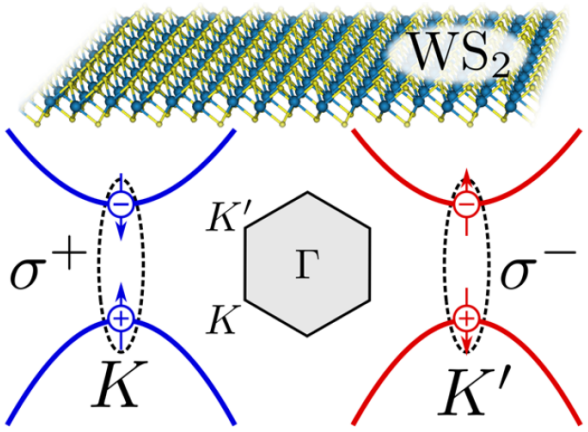

Fig. 1: This figure has been borrowed from [21]. Upper: representation of the atomically thin WS_2 monolayer. Middle: hexagonal structure of the Brillouin zone. Sides: electronic band structure around both valleys K and K' of the Brillouin zone, with the corresponding optical selection rules for left (σ^+) and right (σ^-) circularly polarized excitation.

From all possible TMDs, we will select WS_2 as the paramount 2D layer throughout our work (see Fig. 1). This decision is taken because of two reasons: first, WS_2-exciton energy gaps are larger than the others; second, this is the mainly-used material by our collaborators at ISIS.

There is one more remarkable aspect we must discuss: the direct-band gaps are located in the so-called K and K' valleys of the TMDs hexagonal structured Brillouin zone (see Fig. 1). What is really interesting about these valleys is that through circularly polarized light (left-handed

or right-handed) we can induce optical transitions in, exclusively, one of the valleys (K or K', respectively) (see Fig. 1). This is why TMDs excitons are also called valley excitons and we can talk about valley as a new degree of freedom, opening a window for valleytronics.

We have contextualised the use of WS_2 as our 2D layer so now, we need to know its optical properties. For that purpose, we make use of the experimental data presented in [22] and for which we asked the authors. They provide us with the real and imaginary parts of the dielectric constant, which are related with material conductivity [23] as $\epsilon = 1 + \frac{4\pi i \sigma_{2D}}{h\omega}$, where ϵ is the dielectric constant, h is the width of the material (atomically thin, around 1 nm), ω is the frequency and σ_{2D} is the conductivity. Here there are two things to be noted: we are assuming Gauss convention in the way we wrote the previous expression; and ϵ, σ_{2D} and ω depend on the considered wavelength λ. Since we use Gaussian units, taking a redefinition of the conductivity is more convenient when we want to compute the absorption of the 2D film, which is done in App. D for a general case. This new quantity is $\alpha = 2\pi\sigma_{2D}/c$, being c the light speed in vacuum. Combining both expressions we get: $\alpha = \pi h(\epsilon - 1)/\lambda i$, where we have used that $\omega/c = g = 2\pi/\lambda$.

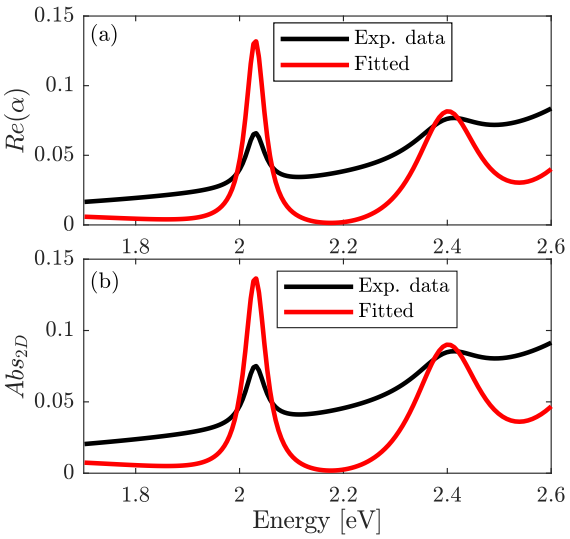

Fig. 2: (a) Real part of α. (b) Absorption of the 2D layer (WS_2).

What really affects to the absorption of the 2D film is the real part of α, i.e., $Re(\alpha)$. That is why, as well as Abs_{2D}, we display this quantity in Fig. 2(a) as a function of energy. We obtain the absorption spectrum expression of WS_2 following the procedure detailed in App. D and shown in Eq. 156 at that appendix. We have considered normal incidence ($\vec{k}^0 = \vec{0}$), the incident polarization $\sigma^0 = p$, the coming medium as vacuum ($\epsilon_I = 1$) and the foregoing as glass ($\epsilon_{II} = 2.25$). We have taken these conditions because this is the configuration used in [21] for their WS_2 absorption spectrum (see Fig. 3). As it can be seen in Fig. 2, there are two different curves for each quantity. This is because experimental data (black) we got from [22] do not produce the same absorption spectrum as [21] presents (see Fig. 3). Therefore, we apply a fitting (red) to these data (see Eq. 1) in order to obtain a better matching between their spectrum and ours.

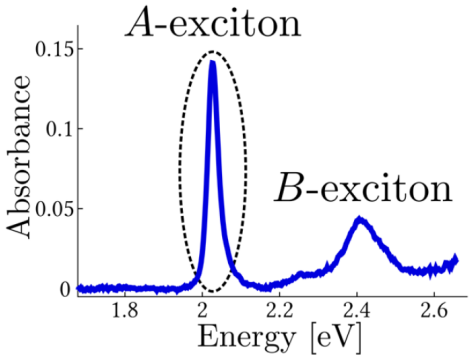

Fig. 3: This figure has been borrowed from [21]. Absorbance spectrum of an exfoliated WS_2 monolayer deposited on a glass substrate.

$$Re(\alpha)_{Fitted} = 3.5\left(Re(\alpha)_{Exp.} - 0.02 \cdot \left(\frac{E(eV)}{1.9}\right)^4 - 2 \cdot 10^{-3}\right) \quad (1)$$

With this fitting we intend to enhance the $Re(\alpha)$, and thus the absorption, around the lower-energy peak. In addition, we also intend to eliminate the background from the whole spectrum provided by the experimental data. Both effects depend on the 2D material quality, which seems better in our collaborators laboratory than where we asked the data for. Therefore, if we look

at the red curve of Fig. 2(b) and we compare it with the spectrum of Fig. 3, we can claim that the agreement between both theirs and ours spectra has significantly improved.

So, we have explained why we use a TMD, in particular WS_2, and we have discussed how we obtain the absorption spectrum of it. As a final point, we must say that the lower-energy absorption peak corresponds to the A-exciton and the higher-energy to the B-exciton, because in the following sections we will mainly focus on the A-exciton.

1.2 Gold dielectric constant

In this section we will characterise the gold slab we will use throughout our work. For this purpose, we will justify the model that we take and we will explain from where the different terms come.

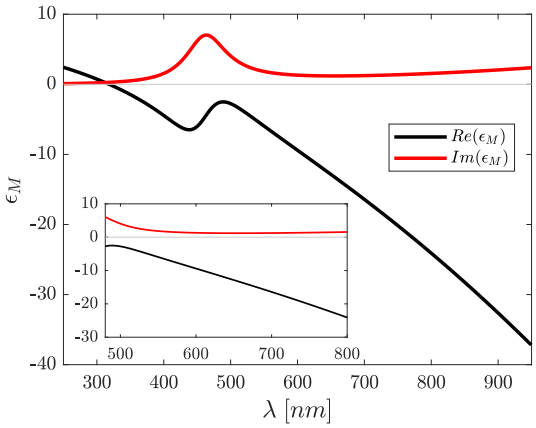

Fig. 4: Representation of ϵ_M of the gold as a function of λ using the expression of Eq. 2 and the parameters given in Table. 1. Inset: zoom in the region of interest.

As stated previously, we will be interested in the near-infrared and optical regimes. It is well-known that, in this frequency range, the dielectric constant of some metals (ϵ_M) can be successfully described by means of the Drude's model, also called free-electron model and that takes into account the intraband transitions [24]. Nevertheless, gold is not well-described via Drude's model in the optical regime. This is why we need to consider also the interband transitions, also referred to as bound-electron effects. We can do this by making use of the Lorentz-Drude model, which basically consists in the addition of Lorentzians (only one for gold case). Therefore, this revised model significantly improves the agreement with the experimental dielectric constant in the near-infrared and optical regimes [25]. Eq. 2 encapsulates this Lorentz-Drude model and Table 1 shows the values for the parameters used in Eq. 2 to characterise the dielectric constant of the gold, ϵ_M.

$$\epsilon_M(\omega) = \epsilon_D(\omega) + \epsilon_L(\omega) = \left(\epsilon_r - \frac{\omega_{P0}^2}{\omega(\omega + i\gamma_0)}\right) + \left(-\frac{\Delta\epsilon_0\ \Omega_0^2}{\omega^2 - \Omega_0^2 + i\omega\Gamma_0}\right) \tag{2}$$

Table 1: Parameters of Lorentz-Drude model for gold. ϵ_r is dimensionless (Gauss convention) and the rest of terms are in eV. These data are adapted from [25].

ϵ_r	ω_{P0}	γ_0	$\Delta\epsilon_0$	Ω_0	Γ_0
5.967	8.729	0.065	1.09	2.684	0.433

So finally, the Lorentz-Drude dielectric constant of gold is shown in Fig. 4. There, we can observe both real and imaginary parts of ϵ_M, as well as zoom in the region where we will mostly work in. Note that the imaginary part of ϵ_M weights the absorption of the metal. If we attend to this in Fig. 4, we observe a maximum around $\lambda \sim 470\ nm$, which corresponds to the characteristic gold absorption.

2 Theoretical model

In this section we will present the theoretical framework where we will work in throughout all this dissertation. Then, we will explain the key features it possesses and when it can be applied. After that, we will move on to discuss the general system to be studied (see Sec. 2.1), as well as the different cases we will consider and their corresponding governing equations. To conclude, we will carry out a comparison between both metal approximations we will handle (see Sec. 2.2).

The method we will apply has been widely used in the study of electromagnetic (EM) properties in different metallic structures [12–14, 26]. It is known as coupled-mode method or modal expansion method. It basically consists on considering both electric and magnetic fields as a superposition of plane waves with different momenta and amplitudes. This is why this method can also be found as momentum expansion method. Then, writing EM fields for every region of space in this way and applying the EM boundary conditions at interfaces between different media, we are able to obtain a set of equations which, if we solve it, returns us the EM fields amplitudes. Therefore, following this pathway we will know the EM fields expressions at any point in the space.

It is also worth noting two aspects. Firstly, these expressions are stationary solutions of Maxwell's equations, so time dependence ($e^{-i\omega t}$) will be removed from this analysis. And secondly, it may be deduced that the convergence of results depends on how many modes we will consider for the superposition. It may also be deduced that if we largely increase the number of modes, the computational cost will indefensibly increase too. Therefore, we will have to make a compromise in order to find well-enough results within a reasonable time.

Before starting with the general-system discussion, we want to make clear that a detailed derivation of the equations is done in App. A, and that here we will only give insight on how to derive them and about some important aspects.

2.1 General system to be studied

In Fig. 5 we display a general representation of the system we will study. The whole space is divided into four different regions labelled by I, II, III and IV. Medium I goes from $z = -\infty$ to $z = 0$ and it is dielectric with constant ϵ_I. Medium II is also dielectric but with ϵ_{II}, and it covers from $z = 0$ to $z = h_1$. In contrast, medium III is a metallic slab drilled, in this case, by holes, which are dielectric. The dielectric constant of the metal is ϵ_M while the holes one is ϵ_{III}. This region occupies from $z = h_1$ to $z = h_2$. Last medium is medium IV, which goes from $z = h_2$ to $z = \infty$, being also dielectric and characterized by ϵ_{IV}.

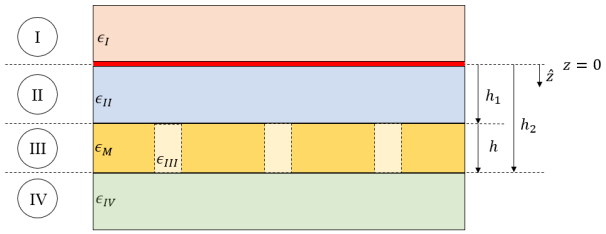

Fig. 5: Scheme of the general system (holes).

At the interface between regions I and II, i.e., at $z = 0$, we place the 2D layer we explained in Sec. 1.1. As we already said, it will be characterised by α, encapsulating the conductivity of the film. So, the distance between this 2D layer and the metallic upper surface is h_1. In addition, metallic slab drillings are not randomly performed. It is a infinitely periodic pattern constituted by equal "unit cells". These unit cells have a certain number of holes distributed along it in a specific way. An example of this is shown in Fig. 25 in App. A, where it is seen that unit cells

are defined by two lengths: p_x and p_y, and every hole will have the same sizes: l_x and l_y. These sizes characterise the shape of the holes but not their distribution into the unit cell, which is defined by two positions and one angle: x_c, y_c and θ_c, being the x and y coordinate of the hole centre and its angle of orientation respect the x axis, respectively. So, this is the general explanation of our system. Now, we will move on to describe some important aspects to be considered.

As we have already stated, we will work with two different types of drillings: holes and dimples. Holes situation has been outlined in the previous paragraphs because we have used it as guiding example. On the other hand, for dimples we need to clarify that region IV does not exist and that h_2 extends to the dimples bottom. And of course, after that, we still have metal. As it can be deduced from the differences between both situations, the quantities we will compute will differ for each case. For holes we will primarily examine transmittance, i.e., the EM energy in region IV; whereas for dimples we will address to absorption or, less frequently, reflectance.

Before continuing, we want to clarify the topic we initiated about the appropiate number of considered Bragg modes in the coupled-mode method. Throughout all this work we will operate with Λ, which will basically be the minimal periodicity of the system, being typically the distance between different holes (or dimples). We will write p_x and p_y as an integer of it, where this integer is the number of holes in each direction because we will typically distribute them along x axis. Then, the number of considered modes is related with $M_x = p_x/\Lambda$ for the x direction and $M_y = p_y/\Lambda$ for the y direction, but only in the modal expansions for regions I, II and IV. Region III is quite special because holes and dimples behave like wave guides. For these, we will only consider one guided mode, the lower energy or fundamental one ($n_x = 0$ and $n_y = 1$, because we will usually take $l_y > l_x$).

The meaning of this choice of modes number will arise now. Regions I, II and IV modes are characterised by a quantity we will call G, which is $G = \{\vec{k}^0 + \vec{G}, \sigma\}$. $\vec{k}^0$ is the incidence momentum vector, which tells us how the incident wave is coming. $\vec{G}$ is a Bragg vector, which lives in the reciprocal lattice of the unit cell and can be written as $\vec{G} = (G_x, G_y)^T = 2\pi \left(\frac{m_x}{p_x}, \frac{m_y}{p_y}\right)^T$. There, m_x and m_y are: $m_x = \{-M_x, -M_x + 1, \ldots, M_x - 1, M_x\} \in \mathbb{Z}$ and $m_y = \{-M_y, -M_y + 1, \ldots, M_y - 1, M_y\} \in \mathbb{Z}$, and characterise the corresponding mode. On the other hand, σ corresponds to the polarization degree of freedom. It can take two values: p or s, which will constitute the polarization basis we will use. This choice of M_x and M_y is well-justified in [13] and it produces the minimal number of modes we need to take in order to be able to excite surface plasmon polaritons (SPPs) on the metal surface. Obviously, the more modes we take, the better is our simulation. However, this is an acceptable (minimal) consideration and the only consequence is a little displacement of the transmittance peaks in larger wavelengths. As we have said, this is enough for us because we are interested in a qualitative approach to the problem, or in other words, we want to achieve a physical explanation and the tendencies of the processes in our system. This is why we use the minimal model [13]. Just as clarifying example, if we have only one hole into our unit cell, thus $p_x = p_y = \Lambda$, $M_x = M_y = 1$, having then three Bragg's vectors for each direction.

The explicit functional form for the modes in regions I, II and IV is

$$\langle \vec{r}_\parallel | \vec{k}_\parallel, p \rangle = \frac{e^{i\vec{k}_\parallel \cdot \vec{r}_\parallel}}{k_\parallel \sqrt{p_x p_y}} (k_x, k_y)^T, \tag{3}$$

$$\langle \vec{r}_\parallel | \vec{k}_\parallel, s \rangle = \frac{e^{i\vec{k}_\parallel \cdot \vec{r}_\parallel}}{k_\parallel \sqrt{p_x p_y}} (-k_y, k_x)^T, \tag{4}$$

where $\vec{k}_{\|} = (k_x, k_y)^T = \vec{k}^0 + \vec{G}$ and $\vec{r}_{\|}$ is a vector of the unit cell. Note that the vectorial character of the previous expressions is determined by the polarization. When $\vec{k}_{\|} = \vec{0}$ the distinction between the case $\sigma = p$ and the case $\sigma = s$ is arbitrary, so we take wilfully that $\langle \vec{r}_{\|} | \vec{0}, p \rangle = (1,0)^T/\sqrt{p_x p_y}$ and $\langle \vec{r}_{\|} | \vec{0}, s \rangle = (0,1)^T/\sqrt{p_x p_y}$. On the other hand, the fundamental mode in region III is expressed as

$$\langle \vec{r}_{\|} | n \rangle = \sqrt{\frac{2}{l_x l_y}} \sin(q_y(y + l_y/2)) \cdot (1,0)^T \quad \text{for } \vec{r}_{\|} \text{ inside the hole and 0 otherwise,} \tag{5}$$

where n only refers to we are considering the n-th hole, but the modes for every hole are the same. Note that, here, the bi-vector and the coordinates ($\vec{r}_{\|}$) belong to the reference framework of the hole, including any possible rotation of this latter (see App. B.2 for a further explanation).

As we stated previously, in this work we will present two different approximations for the metallic slab: it is a perfect electric conductor (PEC) or it follows the surface impedance boundary conditions (SIBC) approximation. First, one supposes that the dielectric constant of the metal is $\epsilon_M = -\infty$, which implies that the EM fields do not penetrate the metal and they are zero at the surface. This also implies that there is no absorption by the metal. On the other hand, the SIBC approximation does consider the EM fields penetration into the metal. This can be understood as the first-order Taylor expansion in $z_s = 1/\sqrt{\epsilon_M}$, where ϵ_M is the actual value of the dielectric constant (see Fig. 4) and not $-\infty$ as happened for PEC (in that case, $z_s = 0$ and it corresponds to the zero-order Taylor expansion). This z_s is used to relate the tangential components of the electric and magnetic fields at the surface of the metal such as $|\vec{E}\rangle = z_s \, |\vec{H} \times \hat{u}_n\rangle$, where $\hat{u}_n$ is an unitary vector orthogonal to the surface and pointing to the inside of the material. As the implementation of the SIBC approximation to vertical surfaces (holes walls) would complicate the calculations, we have decided only to apply it in the horizontal surfaces. However, the effect of field penetration is phenomenologically considered for the vertical surfaces by enlarging of hole size. Since the metal is no more a perfect conductor, the EM field penetrate the material and we do not have the condition of cancelling the fields at the surface. Therefore, this can be seen as an effective enlarging of the holes. We will model it by the use of the skin depth, defined as $\delta = \frac{\lambda \cdot Im(z_s)}{2\pi}$, and we will use it as an addition to the holes length and width but corrected by a phenomenologically estimated parameter, i.e., $l'_{x,y} = l_{x,y} + a\delta$, being $a \simeq 1.25$ for our case [26]. Thus, we have solved the problem of implementing the SIBC approximation for the vertical surfaces. However, the above definition of z_s is perfectly valid when $|\epsilon_M| \gg \epsilon_d$, being ϵ_d the dielectric constant of the sharing-interface dielectric, but as we are not exactly in that situation because of the ϵ_M dependence on wavelength (see Fig. 4), we are going to consider $z_s = 1/\sqrt{\epsilon_M + 1}$ instead of the previous one. This is a next step refinement of the SIBC approximation. Here, 1 corresponds to the vacuum dielectric constant, which will be mainly the sharing-interface dielectric that we will use. Nevertheless, there will be some occasions where we will utilise glass instead of vacuum, but this fact will do not worry us because we only seek a qualitative approach to our colleagues' results [21] and this previous expression is more than enough.

Having all this into consideration, we could start with the derivation of the governing equations for the four cases we have stated: PEC with holes, PEC with dimples, SIBC with holes and SIBC with dimples. However, since the procedure is considerably long, we have decided to put it entirely in App. A and here we will only highlight the key points.

Instead of the magnetic field, we will use other equivalent quantity whose expression in terms of the electric field is just through the modal admittance of the corresponding mode (see Eq. 19 of App. A). We will use Dirac's notation in order to write the modes in the superposition, being well-defined in Eqs. 3, 4 and 5. Then, we will put the fields for every region in terms of some parameters (see Eqs. 28, 29, 30 and 31 of App. A), which encapsulate the weights of each mode

and which are more understandable if we attend to Fig. 26 in App. A. After that, we will make the EM fields to satisfy the boundary conditions at the three interfaces, providing the equations we will solve. But before that, we will carry out a redefinition of some parameters in a way that our unknown quantities then will be the electric field modal amplitudes at both upper and lower metallic interfaces ($\{E_n\}$ and $\{E'_n\}$, respectively). Now, we are ready to present the governing equations for each case:

- PEC with holes, derived in App. A.1:

$$\begin{aligned}(G_{nn}^{I,II} - \Sigma_n)E_n + \sum_{m\neq n} G_{nm}^{I,II}E_m - G_n^V E'_n &= I_{0,n}^{ex},\\ (G_{nn}^{IV} - \Sigma_n)E'_n + \sum_{m\neq n} G_{nm}^{IV}E_m - G_n^V E_n &= 0.\end{aligned} \tag{6}$$

- PEC with dimples, derived in App. A.2:

$$(G_{nn}^{I,II} - \Sigma_n)E_n + \sum_{m\neq n} G_{nm}^{I,II}E_m = I_{0,n}^{ex}. \tag{7}$$

- SIBC with holes, derived in App. A.3:

$$\begin{aligned}(G_{nn}^{I,II} - \Sigma_n)E_n + \sum_{m\neq n} G_{nm}^{I,II}E_m - G_n^V E'_n &= I_{0,n}^{ex},\\ (G_{nn}^{IV} - \Sigma_n)E'_n + \sum_{m\neq n} G_{nm}^{IV}E_m - G_n^V E_n &= 0.\end{aligned} \tag{8}$$

- SIBC with dimples, derived in App. A.4:

$$(G_{nn}^{I,II} - \Sigma_n)E_n + \sum_{m\neq n} G_{nm}^{I,II}E_m = I_{0,n}^{ex}. \tag{9}$$

Our indices (n) correspond to the n-th hole/dimple in the unit cell, so we have two equations per hole for hole arrays and one equation per dimple for dimple arrays. In fact, we could say we have one equation per aperture in the unit cell. Also, the equations for dimples do not present any dependence on $\{E'_n\}$ because it is the electric field modal amplitude at the exit interface, but it is zero.

Now, we must address the meaning of every term that appears in the governing equations: $G_{nm}^{I,II}$, G_{nm}^{IV}, Σ_n, G_n^V and $I_{0,n}^{ex}$. Their expressions are indicated in their corresponding appendices because they vary according to the considered case (see Apps. A.1, A.2, A.3 and A.4). All of them only depend on a handful of known quantities such as the 2D layer conductivity (via α), the modal admittances, some exponentials (dependent on h and h_1) and the overlapping integrals (calculated in detail in App. B). However, what we are really interested in is the physical meaning of them. For a greater understanding it is helpful to take a look to Fig. 6 where we graphically establish a physical relation for them.

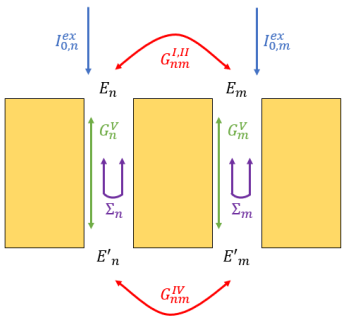

Fig. 6: Physical relevance of the terms that appear in the governing equations.

$G^{I,II}_{nm}$ and G^{IV}_{nm} correspond to the coupling between n-th and m-th apertures throughout any propagating or evanescent modes at the $z = h_1$ and $z = h_2$ surfaces, respectively. $I^{ex}_{0,n}$ is the external illumination, basically governed by the coupling between the incident plane wave (indicated by 0) and the waveguide mode corresponding to the n-th entry aperture. G^{V}_{n} represents the coupling between the $z = h_1$ and $z = h_2$ interfaces but for the same hole (n-th). Obviously this term only appears if we are considering holes, for dimples there is no exit aperture. Finally, Σ_n is related to the bouncing when the EM fields inside n-th hole reach the end of the waveguide.

To conclude, note that this kind of equations has been derived many times [12–14, 26], but always for a simpler system: only the metallic structure. Here, we present the solution introducing also a 2D layer before the drilled slab, resulting in different, and more complex, expressions for almost every term (see App. A).

2.2 Comparison between PEC and SIBC

Firstly, we will discuss, looking at the transmittance (T) spectrum, the differences of considering one of the metal approximations or the other one. Needless to say, if we intend to observe the transmittance spectrum, then we will choose a holey metallic slab. For this purpose, the selected situation is characterised by the following parameters: $\{\epsilon_I = \epsilon_{II} = \epsilon_{III} = \epsilon_{IV} = 1,\ p_x = p_y = 600\ nm,\ l_x = l_y = h = 200\ nm,\ \vec{k}^0 = \vec{0},\ \sigma^0 = p\}$, where σ^0 alludes to the polarization of the incident plane wave. Note that as we are considering every region as vacuum and we are not placing the 2D layer yet, h_1 is meaningless.

In Fig. 7 we take this chosen situation and both spectra are shown: gold as PEC (black) and gold considering the SIBC approximation (red). In the range of wavelengths we will work with (mostly visible regime), PEC approximation is not valid enough because of two reasons: fields do not penetrate the metal surface and plasmons do not emerge. SIBC approximation provides us a framework where these do happen. However, the SIBC approximation also have some details that may become problematic, like it is uniquely a very good approximation if the area of vertical metallic surfaces is much lower than the horizontal ones and the hole size is larger than the skin depth [26]. Both conditions will be loosely satisfied throughout all this thesis. About both spectra comparison, apart from the displacement in wavelengths suffered by the red curve respect the black, we also observe a notorious reduction in transmittance due to the absorption of the realistic metal. And on the other hand, one common feature is the appearance of two different peaks in each spectrum.

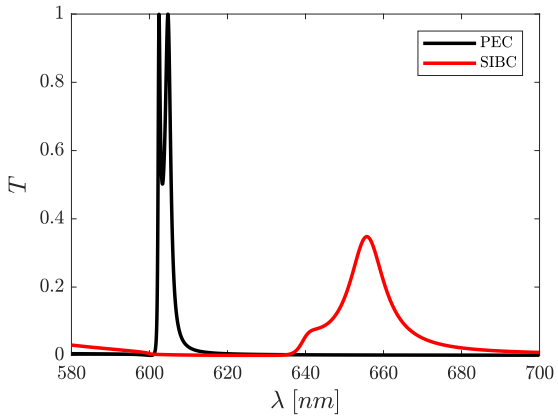

Fig. 7: Transmittance spectrum for both considered approximations (Gold).

Later, we will explain in more detail why it is so necessary that plasmons emerge in our metal surface. So, in short, for the key results of this thesis we will be using the SIBC approximation in order to get as close as possible to the real situation.

It is also important to note that even though PEC approximation is not so good in this regime because of the previous two reasons, there are other wavelengths ranges where it works

well such as microwaves or THz regime [27]. In addition, a more accurate method would be the finite-difference time-domain method (FDTD), but it is unfeasible for these kind of problems, because it is based on real space discretization for Maxwell equations and for the whole structure. Also, there are finite difference and finite element methods (FDM and FEM, respectively), which works with a fixed frequency. However, they do not provide physical insight and the simulations last hours or even days.

Now, we can move on to study the wavelength validity range for which SIBC approximation is reasonable. Here it is convenient to recall the two quantities we talked about when we presented this approximation. These are: $z_s = 1/\sqrt{\epsilon_M + 1}$, and the skin depth $\delta = \lambda \cdot Im(z_s)/2\pi$. As we said, SIBC approximation can be understood as the first-order Taylor expansion in z_s, so we need it to be small. But, what exactly means to be small? Well, from $\lambda \simeq 475$ on, z_s order of magnitude is rather acceptable (see Fig. 8a). In order to provide insight, one can think about how z_s was if we had a PEC: as $\epsilon_M = -\infty$, z_s is essentially zero but imaginary. The real part of z_s is which encapsulates the absorption of the metal. So, it will be desirable to have both real and imaginary parts small, with $Im(z_s) \gg Re(z_s)$. This threshold wavelength condition is complemented by the other quantity, the skin depth δ. We also need it to be small because if we enlarge so much our holes (or dimples) size, these will overlap each other or/and will push the limits of the unit cell. So, we will consider $\delta \in (20, 50)\ nm$ as a permissible skin depth (see Fig. 8b), confirming $\lambda \in (475, 800)\ nm$ as a suited regime to work with. Although there is no problem in extending a bit more the range, up to $\lambda \sim 900\ nm$, as we can observe in Fig. 8.

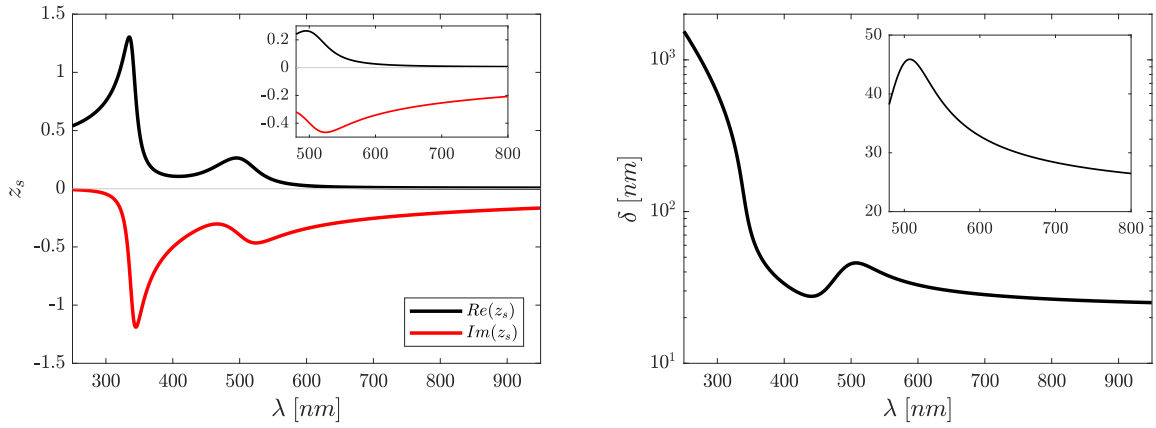

(a) Real and imaginary parts of z_s.

(b) Skin depth (δ).

Fig. 8: z_s and δ in a wide range of wavelengths. Insets: suitable range for SIBC approximation.

3 Checking our model

In this section we will study an ensemble of statements in order to check if our insight about the system is correct or not. For this purpose, we will select a case as simple as possible and we will perform some simulations on it. So, there will be some fixed parameters but others will be free in order to see what happens when we vary them. Before starting with the system characterisation, we want to emphasize that these results will be also used to explain some concepts that will appear throughout this thesis.

Then, first of all, we will consider the metallic slab as a PEC (i.e., $\epsilon_M = -\infty$) and it will be drilled by holes, having thereby the first of all described cases: PEC with holes. So, accordingly, we will address to the system transmittance. In addition, all regions will be vacuum, which

means that $\epsilon_I = \epsilon_{II} = \epsilon_{III} = \epsilon_{IV} = 1$. We will also consider that there is no 2D layer yet, which is equivalent to say that $\alpha = 0$. Our incident plane wave will be characterised by a zero incident momentum, $\vec{k}^0 = \vec{0}$ (normal incidence), while the incident polarization will vary. On the other hand, unit cell dimensions and holes dimensions will remain fixed, being $\Lambda = p_x = p_y = 480\ nm$ and $l_x = l_y = 0.4 \cdot \Lambda = 192\ nm$. About the z-direction distances, $h = 0.2 \cdot \Lambda = 96\ nm$ but h_1 is irrelevant because $\epsilon_I = \epsilon_{II}$ and there is no 2D layer. And lastly, we will take only one hole per unit cell. These are all the fixed quantities. Therefore, hole position ($\vec{r}_c$), hole angle θ_c and incident polarization (σ^0) are susceptible to be varied.

Fig. 9 can be used to understand several details about the unit cell, the incident polarization, the orientation of the holes, etc. We will take Fig. 9a as guide to compare the other ones. This transmittance spectrum is obtained settling the hole at the unit cell centre, forming the lower side of the hole an angle of 0^o respect the x direction and being p the polarization of the incident plane wave. Note that this system has been already studied and the spectrum that we obtain here is alike the presented in [13], as well as the simplified equations we derive taking this specific configuration.

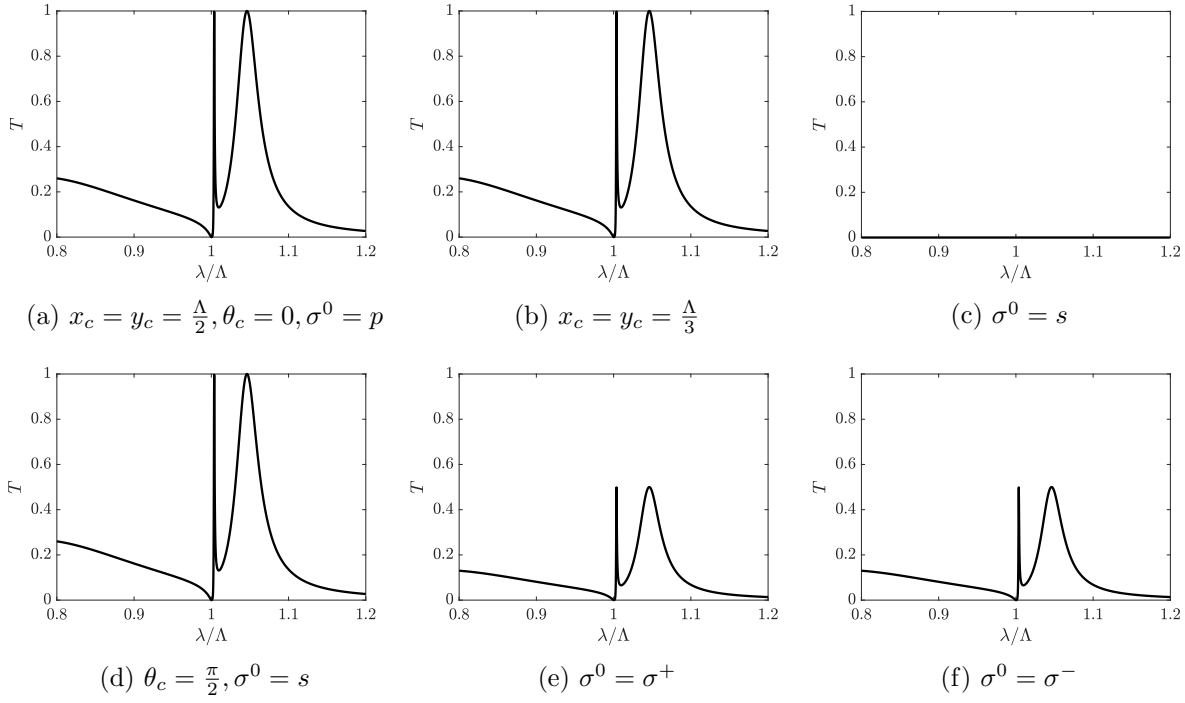

(a) $x_c = y_c = \frac{\Lambda}{2}, \theta_c = 0, \sigma^0 = p$ (b) $x_c = y_c = \frac{\Lambda}{3}$ (c) $\sigma^0 = s$

(d) $\theta_c = \frac{\pi}{2}, \sigma^0 = s$ (e) $\sigma^0 = \sigma^+$ (f) $\sigma^0 = \sigma^-$

Fig. 9: Transmittance spectrum for six different situations. (a) is the pattern situation and in the captions of the rest we specify the performed changes respect the first one.

If we shift the hole to another point on the unit cell, we should expect that nothing changes, given that the unit cell is infinitely periodic into the metallic slab. In fact, this is what happens when we establish the hole centre at $x_c = y_c = \Lambda/3$ (see Fig. 9b).

And, what happens if we take s as the incident polarization? In Fig. 9c we can see that transmittance vanishes. This is because, for normal incidence ($\vec{k}^0 = \vec{0}$) and s polarization, the plane wave mode only has y component, while the hole/waveguide mode only has x component so they cannot couple each other and produce a modal-overlapping which would lead to non-zero transmittance ($I^{ex}_{0,n} = 0$). An analogy could be the experiment of trying to observe linearly polarized light through a polarizer with the opposite linear polarization. And just as remainder, the hole mode only has x component because we uniquely consider the fundamental mode.

However, in Fig. 9d, this previous reasoning is compensated by rotating the hole $\pi/2$ respect x direction. In this new situation, the plane wave mode still only has y component but our hole mode, which only had x component, has been rotated $\pi/2$ and now it only has y component. Then, both modes have the same component and can couple to produce a non-zero transmittance. In fact, the obtained spectrum is equivalent to the first one (see Fig. 9a), which is completely consistent because the plane wave of p polarization (and normal incidence) only has x component and then it perfectly couples with a non-rotated hole.

We will jointly discuss Figs. 9e and 9f. For both we will set the hole at the centre of the unit cell and non-rotated respect the horizontal. But, in contrast with Fig. 9a, we will choose σ^+ and σ^- as the incident polarization, respectively. We have repeatedly said that our polarization basis is conformed by p and s, but we have not explained in detail what this means. We do have remarked that the vectorial character of the projection onto the real space of the plane wave modes is due to the polarization. These have different expressions if we are considering p or s polarization. Then, we can see them as $|p\rangle = (1,0)^T$ and $|s\rangle = (0,1)^T$. On the other hand, σ^+ and σ^-, which correspond to left-handed and right-handed circularly polarized light, respectively, can be also written in terms of these p and s as follows

$$\begin{aligned} |\sigma^+\rangle \equiv |L\rangle &= \frac{1}{\sqrt{2}}(1,i)^T = \frac{1}{\sqrt{2}}(p+is), \\ |\sigma^-\rangle \equiv |R\rangle &= \frac{1}{\sqrt{2}}(1,-i)^T = \frac{1}{\sqrt{2}}(p-is). \end{aligned} \tag{10}$$

And coming back to Figs. 9e and 9f, it is logical to see a reduction of exactly half of transmittance because our hole is only coupling with the half of the incident plane wave: the p part (and both components have the same weight). This fact will be expanded just below.

This notation has some implications when we seek the calculation of quantities such as EM energy fluxes, $I^{ex}_{0,n}$ or just $\delta_{G,0}$. For example, if we tackle the computation of $\delta_{G,0}$, the first thing we have to consider is $\delta_{G,0} = \delta_{\vec{G},\vec{0}}\delta_{\sigma,\sigma^0}$, because 0 here represents the incident state, i.e., $\vec{k}^0$ and σ^0, while G represents $\vec{k}^0 + \vec{G}$ and σ, i.e., a specific mode of the expansion. $\delta_{\vec{G},\vec{0}}$ is straightforward because we just have to take $m_x = m_y = 0$. However, δ_{σ,σ^0} turns trickier when σ^0 is not just p or s because σ indeed is, given it is the basis we work with. Of course, $\delta_{\sigma,\sigma^0} = \langle\sigma|\sigma^0\rangle$. And it implies that when we are computing $I^{ex}_{0,n}$, for example, we will have a non-zero value for $I^{ex}_{(\vec{0},p),n} \propto \langle p|\sigma^0\rangle$ and also for $I^{ex}_{(\vec{0},s),n} \propto \langle s|\sigma^0\rangle$. This type of reasoning is also done when we need to compute some energy fluxes, such as W_{inc} (see App. C), but here the required calculations are like $\langle\sigma^0|Y_0^{I*}\sigma^0\rangle \propto Y^{I*}_{\vec{0},p}\left||\sigma^0\rangle_p\right|^2 + Y^{I*}_{\vec{0},s}\left||\sigma^0\rangle_s\right|^2$, where $|\sigma^0\rangle_{p,s}$ are the p and s components of σ^0. As it can be deduced from the used notation, this is not only valid for σ^+ and σ^- but we can use it for any sort of polarization, writing it in terms of p and s.

To conclude, we will also want to comment what happens when we extend the unit cell and the number of holes. As we already stated, throughout this work we will consider Λ as the typical distance between holes, and when we will add more holes to the unit cell, we will do it increasing as well the unit cell dimension by Λ factors. So, if, for example, we have three holes in the unit cell distributed along x direction, then $p_x = 3\Lambda$ and $p_y = \Lambda$. Obviously, we will consider more Bragg modes for x direction than for y direction, concretely $7 = 3 \cdot 2 + 1$ for x and $3 = 1 \cdot 2 + 1$ for y. But what we really want to remark here is that, if every hole has the same angle and size, then the situation with one hole is equivalent to the previous one with more holes (not shown), leading to equal spectra.

So, to sum up, we have developed insight by studying simple cases: we have learned what happens if we relocate the holes, if we rotate them or if we choose an incident plane wave with a little more complex polarization.

4 Results

In this section we will present the different results we have been extracting over these months of intensive work. Some of them are already known and will be used to test the well-functioning of our simulations and to reinforce our understanding of the diverse exhibited phenomena. Others, in contrast, are novel. Most of them have fruitfully contributed to the enlightening collaboration that we have enjoyed with our colleagues at ISIS. Because, after all, the main objective of both this joint effort and this thesis is to provide a qualitative theoretical framework where their experiments may rely on.

Taking as a reference the experimental setup that our collaborators presented in [21] and that we have discussed with them, we are going to fix some of the system parameters now. The dielectric constants of the media are $\epsilon_I = 1$ and $\epsilon_{II} = \epsilon_{III} = 2.25$. We are coming from vacuum and between the 2D layer and the dimples array we introduce glass as spacer. Note here that they always consider dimples, but when we have to consider holes we will also take $\epsilon_{IV} = 1$. The holes/dimples sizes are $l_x = 100\ nm$ and $l_y = 200\ nm$. The distance between the 2D layer and the metal surface is $h_1 = 5\ nm$. The depth of the dimples or the metallic width, depending on if we are considering dimples or holes, is $h = 80\ nm$. In addition, $\Lambda = 480\ nm$, and if we consider n holes or dimples, the unit cell size will typically be $p_x = n \cdot \Lambda$ and $p_y = \Lambda$, where the holes/dimples will be evenly distributed along x direction at a distance of Λ. And due to the infinitely periodic structure of the metal surface, they will be also evenly distributed along y axis at a distance of Λ. In short, the typical spacing between holes/dimples will be Λ, as well as the y periodicity, but x periodicity will be $n \cdot \Lambda$. Here we want to note that $\Lambda = 480\ nm$ was optimally chosen by our collaborators in order to enhance the plasmonic branches coupling that we will see in Secs. 4.2, 4.3, 4.4. The last two features we are going to fix are the 2D layer and the metallic material: as 2D film we will use the WS_2 that we presented in Sec. 1.1, and as metallic material we will consider the gold introduced at Sec. 1.2, which signifies that we are going to use the SIBC approximation. Note that, as opposed to Sec. 3, here we will not fix the incident momentum completely ($k_y^0 = 0$) because we will probe over it (k_x^0), emerging truly interesting results from these kind of analyses.

4.1 General features

In Fig. 10 we represent the absorption of the entire system for a wide range of wavelengths and incident momenta. This total absorption can be computed in terms of the EM energy fluxes deduced in App. C.3, subtracting the EM flux in the region IV (W_{IV}) to the EM flux in the region I (W_I), and renormalized respect the incident EM flux (W_{inc}): $Abs_{tot} = (W_I - W_{IV})/W_{inc}$. It is important to remark that the considered system presents holes drilling the metallic slab. We only have one hole per unit cell located in its centre and non-rotated ($\theta_c = 0^o$). Also, the incident polarization we have taken is $\sigma^0 = p$ because, since the hole orientation is aligned with the x axis, p polarization provides us a maximum coupling between the modes. In Fig. 10 we can see three highlighted areas, which will be used to discuss the different phenomena that appear in this representation.

The solid red line (see Fig. 10) around $\lambda \simeq 1.05 \cdot \Lambda = 504\ nm$ corresponds to the absorption produced by the golden slab. As a result of considering the SIBC approximation, gold behaves like a realistic metal giving rise to this kind of absorption. This absorption wavelength could have been deduced earlier by means of three different observations, though closely interlinked. Obviously we are talking about the three above figures which cover three related aspects about the considered gold. In Fig. 4 we represented the dielectric constant of the gold, and if we look at the imaginary part of ϵ_M, we observe that its maximum is around $\lambda \sim 500\ nm$. This also applies if we have a look at the real part of z_s in Fig. 8a, we observe that, in the valid range of the SIBC approximation (inset), the maximum is around $\lambda \sim 500\ nm$ too. The last check comes from the skin depth. In the valid range of Fig. 8b we realise that at $\lambda \sim 500\ nm$ the skin depth maximum takes place. Besides, this is completely consistent with the fact that the skin depth quantifies the distance that EM fields penetrate the metallic surface. And obviously, the more they penetrate, the greater is the absorption.

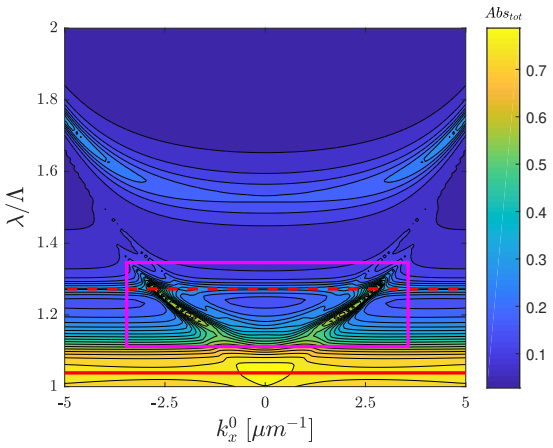

Fig. 10: Total absorption colour-map in terms of the wavelength and the x component of the incident momentum.

On the other hand, the dashed red line (see Fig. 10) around $\lambda \simeq 1.273 \cdot \Lambda = 611\ nm$ corresponds to the absorption produced by the A-exciton of the WS_2-layer. In order to prove that this dashed line corresponds indeed to the mentioned phenomenon, we can focus on the WS_2 absorption, shown in Fig. 2(b). As we said in Sec. 1.1, the lower-energy peak is the A-exciton one, and it is around $2.029\ eV$. This is a bit confusing because of the units so here we set a simple rule of thumb down that we will use now and further on: $E[eV] = 1240/\lambda[nm]$. Then, following this relation we see that $611\ nm \equiv 2.029\ eV$, and therefore we have confirmed the explanation of this absorption. Note that, even though one may not see this momentum-independent absorption by reason of the dashed red line over the colour-map, it can be indirectly observed by the contour lines around it, they flatten at $\lambda \simeq 1.273 \cdot \Lambda$ for all incident momentum. Another point to be noted is that the order of this absorption is much lower than the gold and it can be barely observed because of the colour scale. Nevertheless, we will choose a more appropriate wavelengths range in future plots which will allows us to observe it perfectly, but here we also wanted to show the gold absorption.

To conclude, we will discuss the phenomenon that is highlighted via the pink rectangular box (see Fig. 10). The first two phenomena have one thing in common: independence from the incident momentum, i.e., they hold the same absorption no matter if the incident momentum takes a value or another. So, both are only wavelength dependent phenomena. However, this last point is diametrically opposed, it depends on the incident momentum too. We will use what remains of this section to present just an advancement about the cause of this parabola is the surface plasmon polaritons (SPPs), or just plasmons. We will not treat them here because we will dedicate the next section (see Sec. 4.2) to cover entirely this phenomenon.

4.2 Plasmon dispersion relation

Surface plasmon polaritons (SPPs) are a special type of EM modes that arise near (nanometric scale) a dielectric-metal interface. They are the result of combining a collective excitation of

the metal free electrons ("surface plasmon") with EM waves in the dielectric ("polariton"). They can be implemented in a wide range of scopes of application such as physics (materials), environmental monitoring, chemical sensing or bioimaging, amongst others [9]. This is because their interesting features: a high sensitivity to the dielectric material, a strong variation of the local density of photonic states, the possibility of concentrate light beyond the diffraction limit, a tight spatial confinement or a very fast response [10]. Now, the plasmonic relation dispersion can be written, following our notation, as

$$k_{SPP} = \frac{2\pi}{\lambda}\sqrt{\frac{\epsilon_{II}\epsilon_M}{\epsilon_{II}+\epsilon_M}}, \tag{11}$$

where k_{SPP} is the wavevector modulus of this surface wave, ϵ_{II} corresponds simply to the dielectric constant of the dielectric material and obviously ϵ_M is the metal dielectric constant.

If one plots the relation dispersion (not shown), it can be observed that the plasmonic curve lies to the right of light cone, which means that our incident propagating radiation will not be enough to excite these SPPs. This is because our radiation lies inside the light cone and therefore there is no way of conserving simultaneously parallel momentum and energy. However, there are two main strategies in order to solve this problem: ATR coupling and grating coupling. We will use the latter: grating coupling. Note that both are methods that use light as exciter, but an excitation via electrons can also be performed. All these methods can be found in detail at [28].

Basically, when the photon hits our holes/dimples array, it acquires a new momentum corresponding to a vector of our unit cell reciprocal lattice ($\vec{k}_R$). This can be seen as the plasmonic band gets folded by means of the reciprocal lattice momentum and, thus, it may be possible to find a point of this dispersion relation inside the light cone, satisfying both parallel momentum and energy conservations. This is expressed in Eq. 12,

$$\vec{k}_{SPP} = \vec{k}^0 + \vec{k}_R, \tag{12}$$

where $\vec{k}_{SPP}$ is the vectorial form of the plasmonic dispersion relation, $\vec{k}^0$ is the incident momentum and $\vec{k}_R$ is a vector of the reciprocal lattice (see Sec. 2.1).

In Fig. 11 we represent again the absorption of the entire system for a wide range of wavelengths and incident momenta. Now, the considered system presents dimples instead of holes, which implies that $Abs_{tot} = (W_{inc} - W_{ref})/W_{inc}$, where W_{inc} and W_{ref} are the incident and reflected EM energy fluxes, respectively. We only have one dimple per unit cell located in its centre and non-rotated ($\theta_c = 0^o$). Also, the incident polarization we have taken is $\sigma^0 = p$ and we have not introduced the 2D layer in order to remove the horizontal band at $\lambda \simeq 1.273 \cdot \Lambda$ that we observed in Fig. 10. The last important remark about the system taken in Fig. 11 is that we have chosen $\epsilon_I = \epsilon_{II} = \epsilon_{III} = 1$ because, in this way, above the metallic slab we only have one type of dielectric material. The point is that, if we considered two different dielectrics for region I and II and h_1 was relatively small, Eq. 11 would stop being valid for our system because, in this wavelengths range, the confinement length

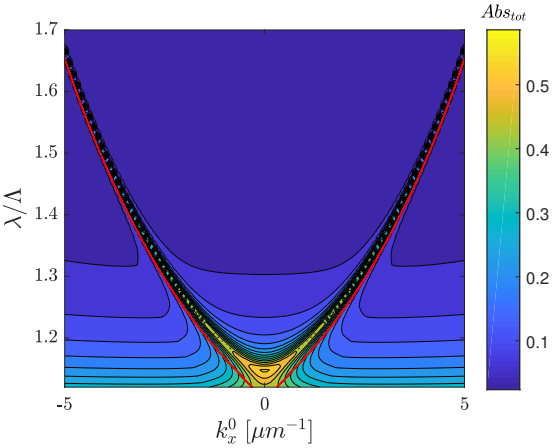

Fig. 11: Total absorption colour-map in terms of the wavelength and the x component of the incident momentum.

of the SPP in the dielectric is on the order of hundreds of nanometers and the SPP would cross the interference between both dielectric media.

Coming back to Fig. 11, the solid red line corresponds to Eq. 12 so we can confirm that our system (colour-map) satisfies the theoretical SPP dispersion relation (red line). In fact, we can see two different branches, which are

$$k_x^0 = \begin{cases} +k_{SPP} - 2\pi/\Lambda & \text{if } k_x^0 < 0, \\ -k_{SPP} + 2\pi/\Lambda & \text{if } k_x^0 > 0. \end{cases} \tag{13}$$

Note that we have only considered the x components of Eq. 12 because in this situation we set k_y^0 and we do not couple with the y direction (dimple at 0^o and p polarization).

With this discussion we have completed the explanation about the phenomenon inside the pink box in Fig. 10 that we presented in Sec. 4.1 too and now we understand why this is a momentum-dependent phenomenon. Finally, one last remark: we have chosen $\epsilon_I = \epsilon_{II} = \epsilon_{III}$ in order to get a better agreement between the simulation and the theoretical expression. However, from now on, we will consider them as different media and therefore Eq. 11 will not be strictly satisfied. Despite all, it will yield an acceptably good agreement and we will only see a little displacement.

4.3 Geometric phase

In this section we will integrate two more levels of similarity respect the experiments carried out by our collaborators in [21]. The first one consists in choosing $\epsilon_{II} = \epsilon_{III} = 2.25$ but keeping $\epsilon_I = 1$ up. This is because in their setup a glass is utilised as spacer between the 2D layer and the dimples array. In fact, this glass is poly(methyl meth-acrylate). This choice of dielectric constants will produce a small displacement when we plot some curves corresponding to the SPP dispersion relation, but as we said in the previous section (see Sec. 4.2), it is not so relevant. The other point we will implement in this section is that we will take six dimples per unit cell instead of one, which means that we will also consider $p_x = 6 \cdot \Lambda$ and $M_x = 6$. In addition, these dimples will not have the same orientation but they will be rotated stepwise along the x axis by an angle $\phi = -\pi/6$. We can observe a representation of this dimples configuration in Fig. 12. We will not introduce yet the 2D layer in order to avoid its characteristic absorption interfering.

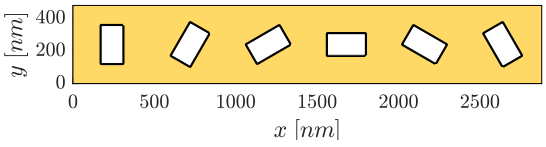

Fig. 12: x-y representation of the unit cell.

Basically, what we intend to accomplish in this section is understand the effect of this kind of rotations over the dimples, and what occurs when we use different incident polarizations (p, s, σ^+ and σ^-).

In [21] they explain this phenomenon: this rotating distribution and its orbital period $(6 \cdot \Lambda)$ establish a rotation vector $\vec{\Omega} = \frac{2\pi}{p_x}\hat{z} = \frac{2\pi}{6\Lambda}\hat{z}$. It combines with σ the spin of the incident light, i.e., plus if it is σ^+ and minus if σ^-, to produce a geometric phase $\Phi_g = -\Omega\sigma x$. This can be deduced from the analysis of the topological Berry phase made in [20]. And, from the gradient of this geometric phase arises a new momentum $\vec{k}_g = -\sigma(2\pi/6\Lambda)\hat{x}$. This implies a new term in the parallel momentum conservation, which is presented in Eq. 14,

$$\vec{k}_{SPP} = \vec{k}^0 + (2\pi/\Lambda)(u\hat{x} + v\hat{y}) + \vec{k}_g, \tag{14}$$

where (u, v) defines the orders of the plasmonic dispersions, being transverse magnetic (TM) polarized along the x direction and transverse electric (TE) polarized along the y axis, respectively.

In Fig. 13 we plot the total absorption as a colour-map depending on the wavelength and incident momentum in x for four different incident polarizations: σ^+ (see Fig. 13a), σ^- (see Fig. 13b), p (see Fig. 13c) and s (see Fig. 13d).

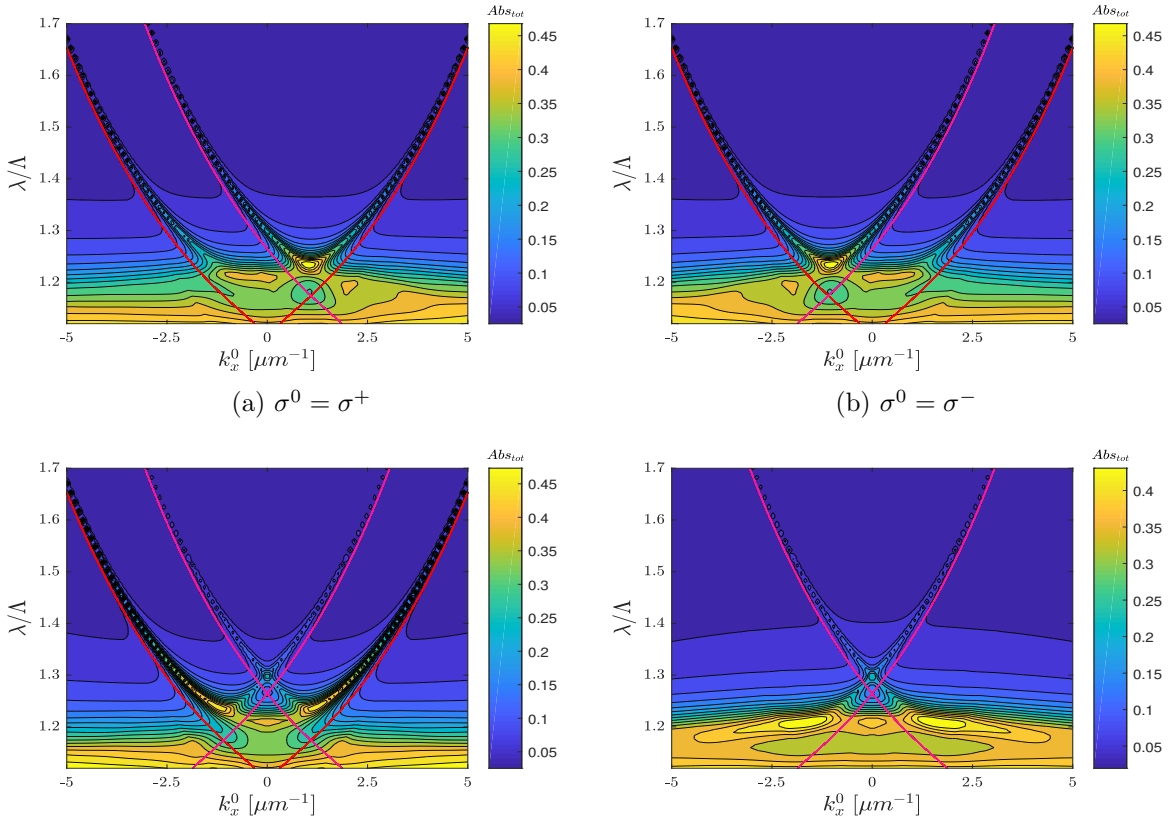

(a) $\sigma^0 = \sigma^+$ (b) $\sigma^0 = \sigma^-$

(c) $\sigma^0 = p$ (d) $\sigma^0 = s$

Fig. 13: Total absorption colour-map in terms of the wavelength and the x component of the incident momentum for four different incident polarizations. Red lines: SPP dispersion relation branches. Pink lines: geometric phase branches.

In Figs. 13 we observe two different effects. The red lines refer to the plasmonic dispersion relation produced by the coupling of the incident light with the reciprocal lattice of our unit cell (see Sec. 4.2), and we will call them grating plasmonic branches because of its origin. And the pink lines correspond to this new topological effect presented in this section. Both presents aspects that are worth noting so we will discuss them separately.

In the first place, the SPP dispersion relation. One could think that as $p_x = 6\Lambda$, then $k_R = 2\pi/6\Lambda$, but nothing could be further from the truth. We need enough momentum to excite the plasmon and this only happens if we take $m_x = M_x = n$ (see Sec. 2.1, this choice is in [13] as the minimal model), i.e., if $k_R = 6 \cdot (2\pi/6\Lambda) = 2\pi/\Lambda$. So, the situation is equivalent to Eq. 13 (only TM modes). Besides, these plasmons branches appear for $\sigma^0 = \sigma^+, \sigma^-, p$ and not for $\sigma^0 = s$. This is because we are only computing the excitation due to incident momentum in the x direction and s is a fully y component vector. Obviously, σ^+ and σ^- branches are less intense because only a half of the polarization gets coupled with the dimples, such is seen in Eq. 10. Another vision about the non-existence of plasmonic branches for the s polarization can be mathematically seen writing p and s in terms of the circular polarizations, which is done in

Eq. 15,

$$|p\rangle = \frac{1}{\sqrt{2}}(\sigma^+ + \sigma^-),$$
$$|s\rangle = \frac{1}{\sqrt{2}i}(\sigma^+ - \sigma^-). \tag{15}$$

From the subtraction which defines s we can also infer the annihilation of the grating plasmonic branches. And not only that, we can infer the enhancement of the grating plasmonic branches for p polarization and the appearance of both geometric phase branches too for p and s.

Secondly, we will discuss the geometric phase branches. There exist an intrinsic link between $u = \pm 1$ and $\sigma = \sigma^{\pm} = \pm 1$, having as a consequence that only one new branch appears if the incident polarization is either σ^+ or σ^-. In other words, a spin-momentum locked branch emerges. Therefore, they appear in $k_{SPP} = k_x^0 + u(2\pi/\Lambda) - \sigma(2\pi/6\Lambda)$. So, depending on the incident handed polarization,

$$\text{for } \sigma^+ : \; k_{SPP} = k_x^0 + 2\pi/\Lambda - 2\pi/6\Lambda,$$
$$\text{for } \sigma^- : \; -k_{SPP} = k_x^0 - 2\pi/\Lambda + 2\pi/6\Lambda. \tag{16}$$

Note that the change of sign in k_{SPP} for σ^- corresponds to the associated branch with $u = -1$ (see lower part of Eq. 13).

This mechanism breaks the left-right symmetry of the modal response of the array, emerging the chirality. One potential application of this chirality would be using a nanophotonic structure where we could control the EM fields in order to make them resonate with chiral molecules, widely used in biology or pharmacology. In Figs. 13a and 13b we observe a geometric phase branch in the position we have predicted. In addition, we can also see a mirror symmetry with respect to $k_x^0 = 0\ \mu m^{-1}$ between both handed polarizations. On the other hand, Figs. 13c and 13d present two geometric phase branches instead of one because of the fact that they are constituted by a part of σ^+ and a part of σ^- (see Eq. 15), so both are excited. Although, obviously, they are much less intense than in $\sigma^{\pm}$ cases.

These last results are, qualitatively, in an absolute agreement with the broken left-right symmetry that our collaborators presented in [21]. Besides, we have also verified it through several results that they and we have been exchanging in this time, as well as via discussion meetings.

4.4 Coupling between WS_2 and plasmons

In this section we will introduce the 2D layer (WS_2). Our objective here is try to observe the coupling between the WS_2 excitons and the geometric phase excited plasmon. From the fact that the 2D layer takes part in this coupling, instead of looking at the total absorption we will turn our attention to the absorption of the 2D film $Abs_{2D} = (W_I - W_{II})/W_{inc}$, where W_I is the EM flux of the region I, W_{II} is the EM flux of the region II and its subtraction is normalized by the incident EM flux W_{inc}. We will maintain the dimples rotated in the same way we did in the previous section (see Sec. 4.3), and we will also keep glass as spacer. On the other hand, since we have seen that σ^+ and σ^- present mirror symmetry, we will only focus on σ^+, i.e., the left-handed circular polarization.

In Fig. 14 we plot the absorption of the WS_2 layer as a function of the wavelength and for thirty incident momenta: they are linearly spaced from $k_x^0 = -1.5\ \mu m^{-1}$ to $k_x^0 = 3.5\ \mu m^{-1}$ starting at the bottom and going upwards. In Fig. 14 we clearly observe the A-exciton peak

around $\lambda \simeq 1.27 \cdot \Lambda$, which is characteristic of the 2D layer. On the other hand, we also observe two of the three branches that we had in Fig. 13a, but just because of the incident momentum range. However, the order of magnitude of these branches is much lower than Fig. 13a ones, because in the 2D layer absorption we only note the coupling with this film and not the full plasmons absorption.

Despite all, we can observe a noteworthy feature more in Fig. 14, the convergence of the geometric phase plasmonic band into the A-exciton band. It occurs around $\lambda \simeq 1.27\Lambda$ and $k_x^0 = 1\ \mu m^{-1}$ ($Abs_{2D} \sim 1.5$, although it does not correspond to the absorption itself). This behaviour was achieved experimentally by our collaborators in [21], and here we present a theoretical framework where it is possible to predict it.

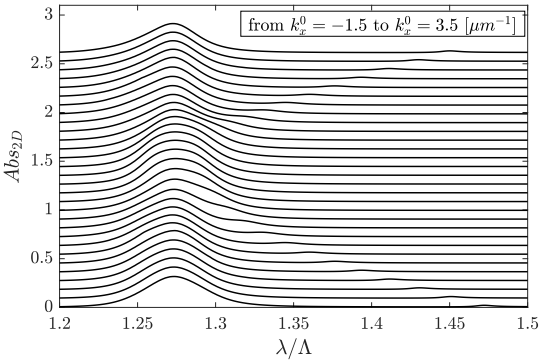

Fig. 14: Absorption of the 2D layer respect wavelength, for some values of x incident momentum and $\sigma^0 = \sigma^+$.

It is also important to clarify that the lower plasmonic branch corresponds to the spin-momentum locked SPP branch generated by the geometric phase; while the upper branch corresponds to one of the grating plasmonic branches. Obviously, the convergence that we are interested in is the spin-momentum locked branch into the A-exciton band, because this is the one due to the left-handed polarization, breaks the left-right symmetry and provides chirality to our system. The other branch, in contrast, also appears equally when we consider the other handed polarization so it is not so relevant.

The last point we want to remark here is the relevance of taking $\Lambda = 480\ nm$ that we advanced in Sec. 4. This optimal Λ produces that the convergence of all plasmonic branches takes place resonantly around the A-exciton band of the WS_2-layer. This fact is also explained in [21].

4.5 Varying several parameters

Once we have reviewed and reproduced the main result of [21], we can use our theoretical framework with the aim of enhancing the coupling between the 2D layer and the spin-momentum plasmonic modes. With this objective in mind, we will select different parameters of our system and we will study its influence over the coupling separately. In particular, we will consider five distinct parameters to vary: the depth of the dimples (h), the distance between the 2D layer and the upper surface of the dimples array (h_1), the dielectric constant of the spacer ($\epsilon_{II,III}$), the ratio between the dimples lengths (l_y/l_x) and the number of dimples (n).

As we observed in Fig. 14 from Sec. 4.4, the plasmonic effect is not too marked. However, there exists a simple way of obtaining an amplification of the effect, while maintaining the physical origin of the phenomena and the main dependences. We will remove the imaginary part of the metal dielectric constant, causing that the plasmons cannot be absorbed by the metal and that their only mechanism plasmon loss is radiation. Obviously, this will have as a consequence the decrease of the total absorption due to the plasmons, but it will do enhance the absorption of the 2D layer.

Note that this is not experimentally plausible and we do not intend to pretend that these results will be true results. We just want to use them as a guide to improve our system configuration and to probe the spectrum dependence on the parameters that can be experimentally modulated. In Fig. 15 we display what happens if we take $Im(\epsilon_M) = 0$ and the consequence is obvious: a remarkable enhancement of the plasmonic branches.

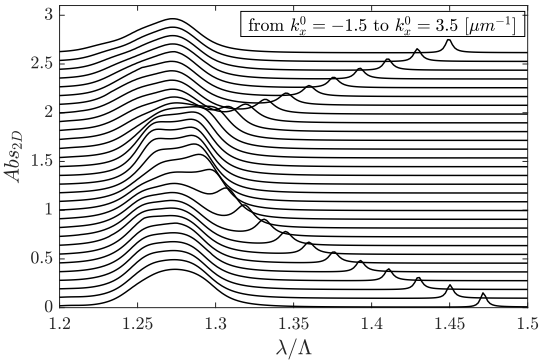

Fig. 15: Absorption of the 2D layer respect wavelength, for some values of x incident momentum, $\sigma^0 = \sigma^+$ and considering the same configuration as in Fig. 14 but taking $Im(\epsilon_M) = 0$.

We will take the absorption of the 2D layer shown in Fig. 15 as a pattern plot to compare the different variations we will carry out in the following sections. We will hold all parameters fixed except for which varies in each section. Recalling these parameters: $\epsilon_I = 1$, $\epsilon_{II} = \epsilon_{III} = 2.25$, $n = 6$, $\Lambda = p_y = 480\ nm$, $p_x = 6 \cdot \Lambda$, $l_y = 2 \cdot l_x = 200\ nm$, $h = 80\ nm$, $h_1 = 5\ nm$, $\sigma^0 = \sigma^+$ and $k_y^0 = 0\ \mu m^{-1}$. The dimples distribution along the unit cell is the same as Fig. 12 shows, with a rotation of $\phi = -\pi/6$ stepwise.

We can easily explore lower and greater values through our simulations. In this sense, they would not need to fabricate each different configuration to test them because we will give to them a bit more of perspective about the problem.

Varying h

Firstly, we are going to study what happens when we vary the depth of the dimples. For our experimental collaborators, $h \sim (60 - 100)\ nm$, and this is the reason why we chose $h = 80\ nm$. It is not so correct to select a very small depth because when $h < 50\ nm$ the metal partially becomes transparent. Thus, we choose $h = 60\ nm$ and $h = 100\ nm$ in order to observe the dependence of the coupling with respect the dimples depth.

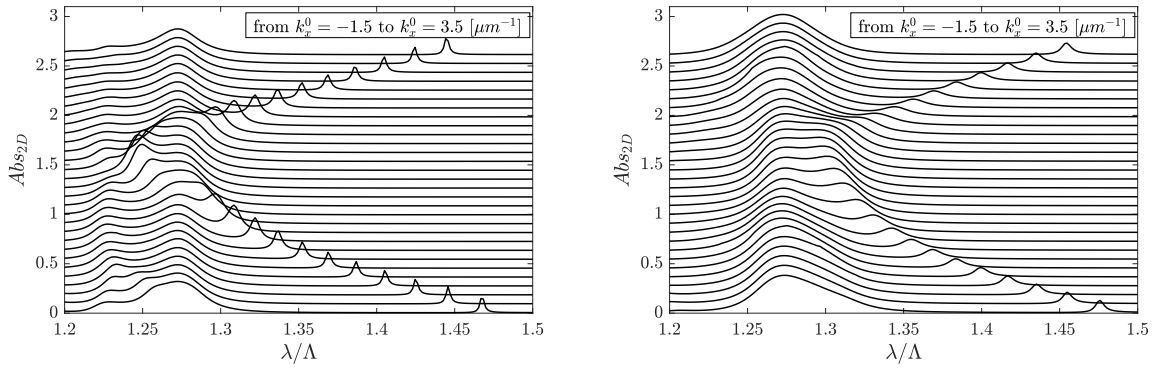

(a) $h = 60\ nm$ (b) $h = 100\ nm$

Fig. 16: Absorption of the 2D layer respect wavelength, for some values of x incident momentum, $Im(\epsilon_M) = 0$ and for two h (left and right).

If we compare Figs. 16a, 16b and 15 we can observe several aspects to be remarked. First, the greater h is, the more the plasmonic branches suffer a displacement towards greater wavelengths. This is very important in order to improve the coupling because we would need to

approach the geometric branch as close as possible to the A-exciton peak band. Having in mind this behaviour at the three noted figures, may be an intermediate step between Fig. 15 and Fig. 16b is even more appropriate: $h = 90\ nm$ would be our choice (not shown). On the other hand, the second dependence on the dimples depth that we can observe in these figures is the flattening of the plasmonic branches if we increase h. In order to enhance the coupling it is more convenient to have the peaks as heightened as possible, therefore, this leads to reassert our choice of $h = 90\ nm$ instead of larger depths.

Varying $\mathbf{h_1}$

Secondly, we are going to discuss the behaviour of the system as a function of the distance between the WS_2 layer and the upper surface of the metallic slab. Experiment [21] were done at $h_1 = 5\ nm$. The effect of having a smaller or larger distance can be studied by considering two different cases: $h_1 = 1\ nm$ and $h_1 = 15\ nm$.

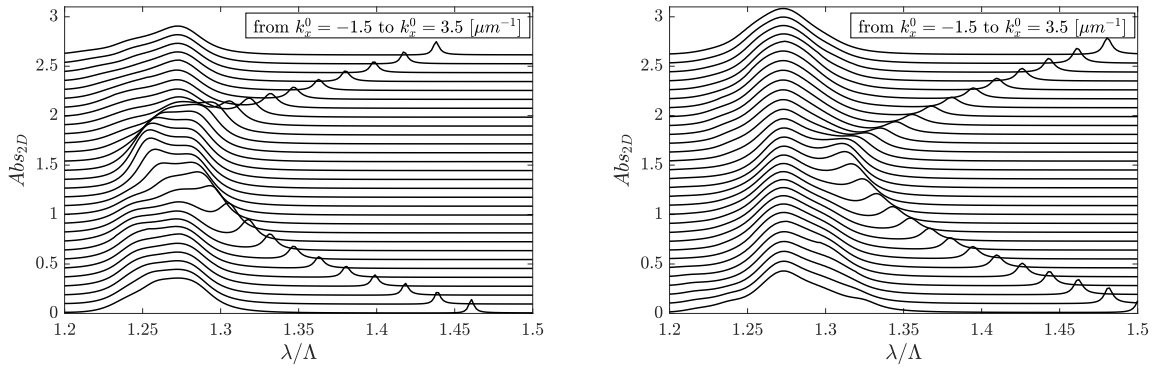

(a) $h_1 = 1\ nm$ (b) $h_1 = 15\ nm$

Fig. 17: Absorption of the 2D layer respect wavelength, for some values of x incident momentum, $Im(\epsilon_M) = 0$ and for two h_1 (left and right).

As what happened when we treated the previous parameter, here we have two aspects to be remarked (see Fig. 17). The first one is that when we increase the parameter h_1 we observe a displacement of the plasmonic branches into greater wavelengths. Likewise, we have to find the parameter which provides us the better convergence of the geometric branch into the A-exciton peak band, and obviously, without crossing it. So, something between $h_1 = 5\ nm$ (see Fig.15) and $h_1 = 15\ nm$ (see Fig. 17b) would be ideal. On the other hand, the second aspect to be discussed is completely opposed to the behaviour of h that we studied in the previous section. In this case, when we increase h_1 we observe an heightening of the plasmonic branches. This could be thought as counter-intuitive: how is it possible that the coupling increases when we move the 2D layer away from the dimples array, where the plasmons emerge? We ascribe this phenomenon to the fact that the plasmon parallel electric field (x and y components) is greater at a certain distance from the metallic slab than just above it, and it is this plasmon parallel electric field which couples with the 2D layer. For all this, we have to choose an h_1 whose value is great enough to get an enhancement of the coupling but, at the same time, not too large because we want to keep the spin-momentum locked branch near the A-exciton band and when we increase h_1 this branch gets shifted to larger wavelengths. Hence, the most appropriate value for us, after probing between $h_1 = 5\ nm$ and $h_1 = 15\ nm$, is $h_1 = 10\ nm$ (not shown).

Varying $\epsilon_{\mathbf{II,III}}$

In this section, we are going to study about another feature that we can modify with the objective of enhancing the coupling. We can take different values for the dielectric constant of the spacer ($\epsilon_{II,III}$) in order to analyse how it affects the absorption spectrum of the 2D layer. But before starting with this test, there is an aspect that we must remark. Unlike previous parameters (h and h_1), the dielectric constant of the spacer is not so clearly selectable because it depends on the chosen material. For example, it is not like h, for which we can decide to drill deeply the metallic slab and it is solved. Here, we have the constraint of if there exists a dielectric material with the selected dielectric constant. However, we choose $\epsilon_{II,III} = 1.5$ and $\epsilon_{II,III} = 3$ to see the spacer dependence.

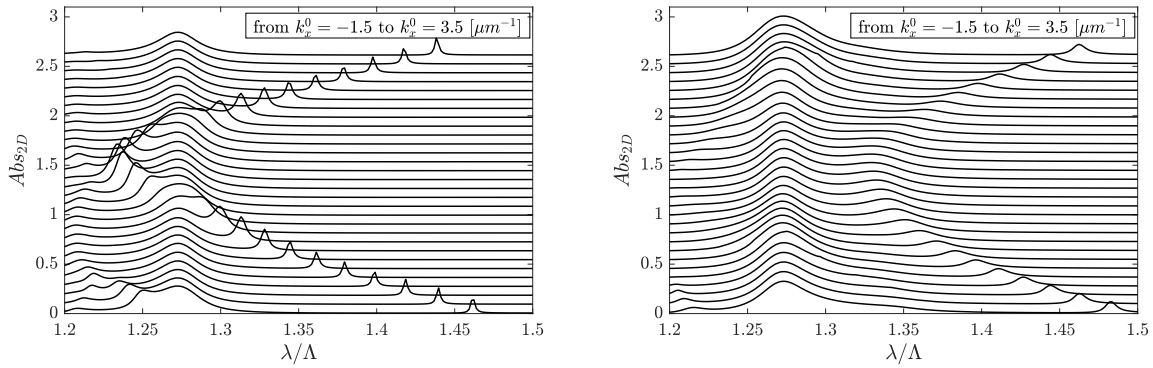

(a) $\epsilon_{II,III} = 1.5$ (b) $\epsilon_{II,III} = 3$

Fig. 18: Absorption of the 2D layer respect wavelength, for some values of x incident momentum, $Im(\epsilon_M) = 0$ and for two $\epsilon_{II,III}$ (left and right).

Again, we attend to Figs. 18a, 18b and 15 to compare them. We observe the same two phenomena as we studied the dependence on h. If we reduce the dielectric constant of the spacer we observe a displacement of the plasmonic branches into lower wavelengths, even crossing the A-exciton band, just like occurs with h. In addition, when we increase this dielectric constant we notice a little flattening of the plasmonic branches peaks. So, again, we have to make a compromise: we need a small enough dielectric constant to keep a non-flattened and heightened plasmonic branches but, at the same time, we also need a large enough $\epsilon_{II,III}$ so that the spin-momentum locked branch converges to the A-exciton band and get an acceptable coupling. Having this considerations in mind we propose $\epsilon_{II,III} = 2.5$ (not shown) as the optimal dielectric constant of our spacer. On the other hand, coming back to the argument about the material constraints, we accept that if it is not possible to find any spacer with $\epsilon_{II,III} = 2.5$, the poly(methyl meth-acrylate), which, as said has $\epsilon_{II,III} = 2.25$, is rather reasonable.

Varying $\mathbf{l_y/l_x}$

Now, we are going to treat the differences derived from choosing distinct sizes for the dimples. In order to simplify the analysis, we will keep $l_x = 100$ fixed and we will only vary l_y. There is a little aspect here that we must remark: we have strong restrictions for l_y because, if we enlarge it too much, dimples may overlap each other or/and push the limits of the unit cell. This limiting value, for $l_x = 100\ nm$, is $l_y = 390\ nm$. Perhaps it does not seem very large to overlap or push the limits but we recall that the field penetrates into the metal a distance of the order of the skin depth into the vertical surfaces. As values to discuss, we have chosen $l_y = 150\ nm$ and $l_y = 250\ nm$.

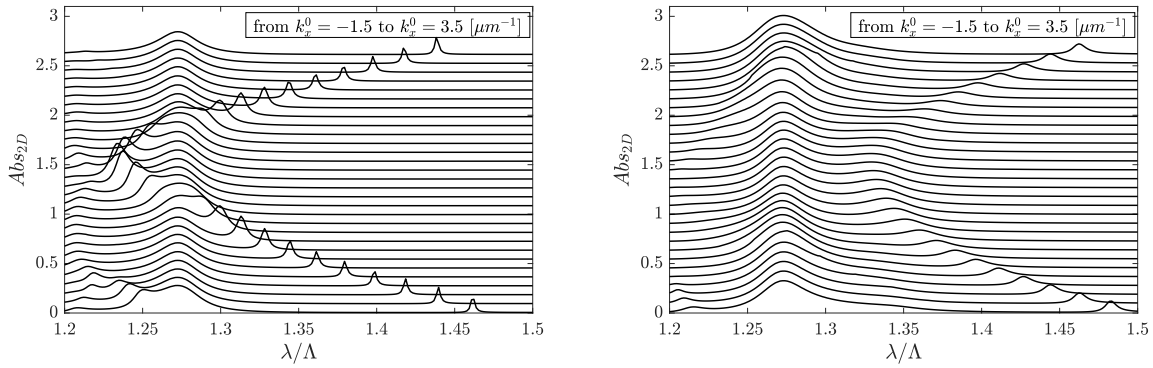

(a) $l_y/l_x = 1.5$ (b) $l_y/l_x = 2.5$

Fig. 19: Absorption of the 2D layer respect wavelength, for some values of x incident momentum, $Im(\epsilon_M) = 0$ and for two l_y/l_x (left and right).

Looking at Figs. 19a, 19b and 15 we can deduce that the two phenomena emerging from these changes are the same as before. Again, we observe a displacement into greater wavelengths when we increase l_y respect l_x. And of course we also appreciate a little flattening of the plasmonic branches peaks for the same increase. And since we need the geometric phase branch converging into the A-exciton band and also to be enhanced enough, we choose $l_y = 200\ nm$ as our proposition after having probed the intermediate options.

Varying n

Finally, we are going to study the influence of the number of dimples in the coupling between the spin-momentum locked branch and the 2D layer A-exciton band. This section can be split in two parts: in the first one we will discuss the dependence on the number of dimples in the same way that we did with the other parameters and we will explore the geometric phase branch dependence on the number of dimples; and finally, we will examine a novel type of unit cell that may provide new intriguing effects.

The first point we must clarify is that if we change the number of dimples, then the angles θ_c of the dimples themselves also change. When we had $n = 6$, the stepwise angle was $\phi = -\pi/6$ and the shape of its distribution along the unit cell was shown in Fig. 12. However, if we have an arbitrary number of dimples, n, the angle that we rotate stepwise along the x axis is $\phi = -\pi/n$. Here, we are not going to show another unit cell representation for each considered n, but it is easy to imagine them. If we increase the number of dimples, apart from p_x increases linearly too, the rotation of dimples performed along the x axis becomes smoother. In the same way, if we reduce the number of dimples, this rotation gets more discrete, in the sense that the angle steps between two of them are more marked.

As we have seen in Sec. 4.3, the geometric phase also depends on the number of dimples in these configurations. For an arbitrary n, this is $\vec{k}_g = -\sigma(2\pi/n\Lambda)\hat{x}$. This implies that, for σ^+, the geometric branch will appear in $k_x^0 = k_{SPP} - 2\pi/\Lambda + 2\pi/n\Lambda$. So, the more we increase the number of dimples, the smaller is the distance (in momentum) between the geometric phase branch and its corresponding grating plasmonic branch ($\sigma^+ \Rightarrow u = +1$).

We can observe this fact in Fig. 20. The geometric phase branch (at the middle) gets closer to the left branch with this tendency. In this Fig. 20 we consider large range in number of dimples: from $n = 3$ to $n = 20$. The case $n = 1$ is not considered because it is not possible

to perform a rotation along the dimples in the x axis when we only have one. The case $n = 2$ is not either considered; in this case, the first dimples would be at $\theta_c^{(1)} = 0^o$ and the second at $\theta_c^{(2)} = 90^o$, this blocks the left-right symmetry breaking and thus, left and right-handed circular polarizations produce equivalent spectra.

Once we have studied the behaviour of the geometric phase branch respect the number of dimples, we can show the absorption of the WS_2 layer for several specific cases. However, instead of using the same type of plots as in the previous parameters discussions, we are going to use a colour-map to observe more clearly the dependence on wavelengths and x incident momentum. We choose $n = 3$ and $n = 9$ as values to compare the different spectra. In Fig. 13a we shown this kind of colour-map for $n = 6$ and this incident polarization, although there are two main differences: there, we plotted the total absorption of the system and we did not placed the 2D layer yet. Then, it is not possible to directly compare that figure with Figs. 21a and 21b here. However, we can use it as reference, because the branches positions and shapes are not so affected, particularly when we are considering the model without metal absorption (setting $Im(\epsilon_M) = 0$).

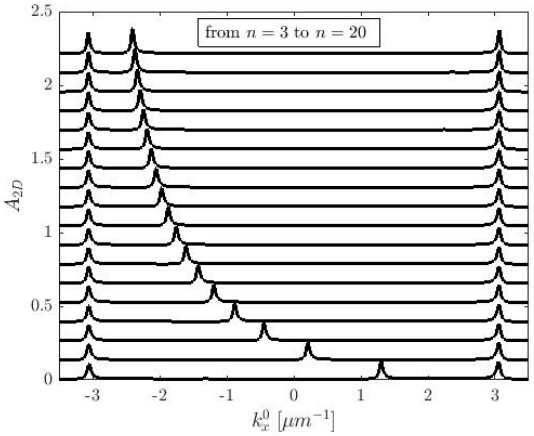

Fig. 20: Absorption of the 2D layer respect x incident momentum, for $\lambda = 1.4\Lambda$ and some values of n, and taking $Im(\epsilon_M) = 0$.

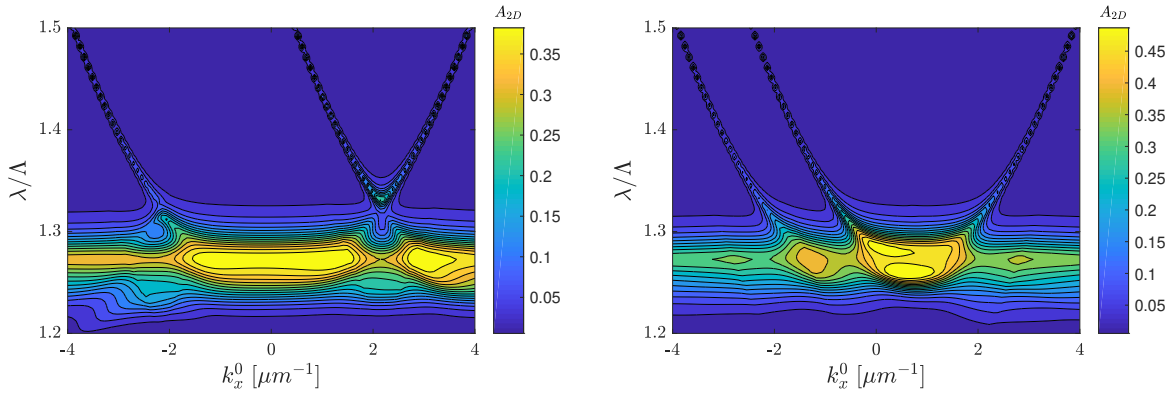

(a) $n = 3$ (b) $n = 9$

Fig. 21: 2D layer absorption colour-map in terms of the wavelength and the x component of the incident momentum for two different number of dimples per unit cell, and $Im(\epsilon_M) = 0$.

In Figs. 21a and 21b there is one main aspect to be emphasized, but from it more arise. Comparing both figures we can observe that the geometric phase branch (the middle one) has suffered a displacement getting closer to its parallel grating plasmonic branch when we have increased n from 3 to 9. This is because of the dependence explained just above. Nevertheless, this phenomenon has two indirect effects in these spectra. First, we recall the expression for the geometric phase branch: $k_x^0 = k_{SPP} - 2\pi/\Lambda + 2\pi/n\Lambda$, and the associated plasmonic branch: $k_x^0 = k_{SPP} - 2\pi/\Lambda$, which are parallel because they only differ in a constant term. This provokes that while we increase n, the geometric phase branch gets closer not only to the plasmonic branch but to the A-exciton band too, which is ideal in order to enhance the coupling. Second,

due to the interaction between the geometric phase branch and the A-exciton band when the first gets closer to the second, the order of magnitude of Abs_{2D} increases, which is also excellent for the coupling.

Therefore, taking into account these previous effects one can think about what is the optimal number of dimples to achieve this coupling. Obviously, $n = 3$ is not enough because we do not reach the convergence of the geometric phase branch into the A-exciton band, they stay separated (see Fig. 21a). However, considering $n = 5$ (not shown) we do reach it and, in fact, it provides some advantages over larger n's. If we increase a lot the number of dimples per unit cell, the computational cost would increase dramatically and the experimental setup would be more difficult to implement. So, we find that $n = 5$ is a good compromise and we will use it to explore the last point.

Finally, we will introduce a new type of unit cell: instead of distributing the dimples only along the x axis, we will expand the unit cell not only in the x axis but also in the y axis and we will distribute them along both (x and y). In this way, we will rotate the dimples stepwise along both axis, having as a result the unit cell shown in Fig. 22. Note that here we have considered $n = 25$ dimples (5×5). The stepwise rotation that we have carried out consists on $\phi = -\pi/5$ in both directions. Obviously, $p_x = p_y = 5 \cdot \Lambda$ and the dimples centres are located at the middle of the corresponding sub cells $\Lambda \times \Lambda$. To conclude, our last result is shown in Fig. 23, where we present the 2D layer absorption for a classic unit cell of five dimples (see Fig. 23a) and for the new type of unit cell presented in Fig. 22 (see Fig. 23b).

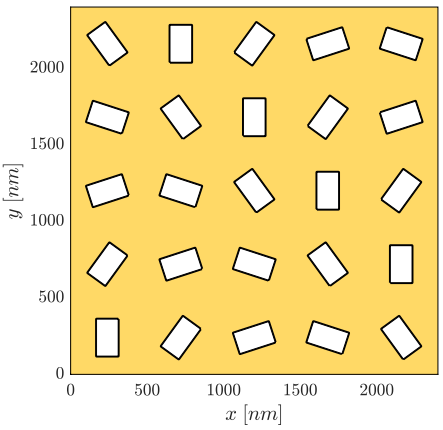

Fig. 22: x-y representation of the unit cell.

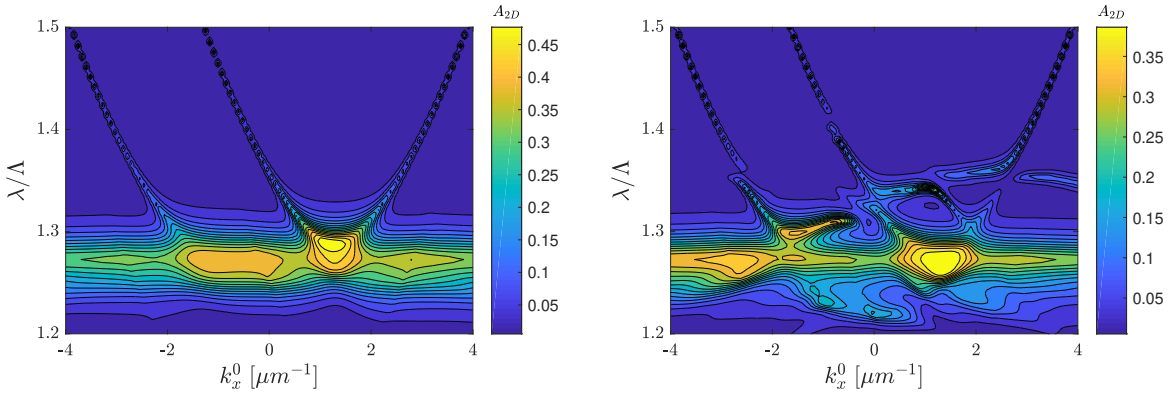

(a) $n = 5$

(b) $n = 25$, dimples configuration as in Fig. 22.

Fig. 23: 2D layer absorption colour-map in terms of the wavelength and the x component of the incident momentum for two different number of dimples per unit cell, and $Im(\epsilon_M) = 0$.

Here, we intend to compare both absorptions in order to understand the effects of modifying the unit cell form in this way. Looking at Fig. 23a and after that, at Fig. 23b we can guess that, broadly speaking, every branch is in the same position and has the same shape, except for some

dissimilarities around $\lambda \sim 1.35 \cdot \Lambda$ in Fig. 23b. Besides, the order of magnitude of this absorption has been reduced due to the lack of coupling between the geometric phase branch and the A-exciton band. But here there is one important point: we have also performed rotations along the y axis, which implies that a new geometric momentum emerges with the same characteristics as the previous but in the y direction. In order to analyse the behaviour of this new effect we would need to probe k_y^0 as well as k_x^0. The band structure may present very interesting topological effects which we leave for future work. Despite all this, these novel type of unit cells opens up a new range of possibilities to study the left-right symmetry breaking, the "strong" coupling, the spin-momentum locking and, in essence, the behaviour of the system in relation to the polarization handedness. Besides, the possibility of performing different-sign stepwise rotations appears: we may use $\phi_x = -\pi/5$ and $\phi_y = \pi/5$ being the x and y step rotations in those directions, respectively. This would provide us a different-sign geometric momenta for each direction, offering sensitivity to the handedness but using a single setup.

Conclusion

Throughout this Final Master's Thesis we have been approaching stepwise to the configuration presented and studied by our collaborators at ISIS in [21]. We have developed a theoretical framework from where we have qualitatively explained the phenomena that they observed experimentally. This analysis has proven to be remarkably satisfactory for all of us. As a result of this collaboration, we have improved our understanding of this system and of the physics behind it.

More specifically, we have studied the relevant (for our purposes) properties of the tungsten disulfide, which was chosen as the atomic-width material that we will use for our work due to its suitable features. Besides, we also discussed in depth the relevance of considering the metallic nanostructure as gold, because it is well suited for nanoplasmonics [10].

On the other hand, we have successfully derived the governing equations of the system. As check, we also considered a simpler system and deduced its equations from the general ones, recovering the expressions present in the literature [12,13]. In addition, we have also performed simplified simulations in order to check our intuition about the problem.

And lastly, we considered the full system shown in [21]. We have satisfactorily identified in our simulations all the effects that our collaborators discussed in their paper: we have observed the gold typical absorption around $\lambda \simeq 500\ nm$, we have also reproduced the absorption owing to the tungsten disulfide A-exciton around $\lambda \simeq 611\ nm$, we have checked that the SPPs dispersion relation is in excellent agreement with our simulations, and we have derived from the Berry phase and observed in our plots the geometric phase momentum, which is accountable for the spin-momentum locking referred in [21].

The last part of this thesis has been about studying the coupling between the 2D layer and the geometric phase dependence on different parameters that can be subject to change. This discussion has been extremely useful in order to shed light on the potential modifications that our collaborators could carry out to enhance this coupling. A quick recap of these modifications is presented here: to increase the dimples depth, to increase the distance between the 2D layer and the metallic array, to increase the spacer dielectric constant, to keep the dimples size and to reduce the number of dimples (and for further steps, consider $n \times n$ unit cells). Our experimentalist colleagues are now manufacturing samples along these guidelines in order to perform new experiments soon.

In spite of the broad study that we have carried out throughout this dissertation, several areas still remain unexplored. Here, we intend to recall and raise those ones that would be interesting and worthwhile to direct our efforts to. After having studied the coupling dependence on the different parameters individually, we should perform an optimisation of this coupling via the gradient descent method considering all the parameters simultaneously. We could also consider the new type of unit cell presented in Fig. 22 and study exhaustively additional effects that it could exhibit: probing k_y^0 as well as k_x^0, changing the incident polarization or modifying the rotation direction depending on the axis, amongst many other things. And in order to provide some quantitative results, we could run several simulations considering a larger number of modes in the expansion. These simulations would return us spectra with greater accuracy and that could be useful regarding the strong coupling quantification. So, to sum up, these are the areas that we will cover in a future work.

Bibliography

[1] K. S. Novoselov, A. K. Geim, S. V. Morozov, D. Jiang, Y. Zhang, S. V. Dubonos, I. V. Grigorieva, and A. A. Firsov. Electric field effect in atomically thin carbon films. *Science*, 306(5696):666–669, October 2004.

[2] K. F. Mak and J. Shan. Photonics and optoelectronics of 2d semiconductor transition metal dichalcogenides. *Nature Photonics*, 10(4):216–226, March 2016.

[3] T. Low, A. Chaves, J. D. Caldwell, A. Kumar, N. X. Fang, P. Avouris, T. F. Heinz, F. Guinea, L. Martin-Moreno, and F. Koppens. Polaritons in layered two-dimensional materials. *Nature Materials*, 16(2):182–194, November 2016.

[4] YJ. Chen, J. D. Cain, T. K. Stanev, V. P. Dravid, and N.l P. Stern. Valley-polarized exciton–polaritons in a monolayer semiconductor. *Nature Photonics*, 11(7):431–435, June 2017.

[5] S. Dufferwiel, T. P. Lyons, D. D. Solnyshkov, A. A. P. Trichet, F. Withers, S. Schwarz, G. Malpuech, J. M. Smith, K. S. Novoselov, M. S. Skolnick, D. N. Krizhanovskii, and A. I. Tartakovskii. Valley-addressable polaritons in atomically thin semiconductors. *Nature Photonics*, 11(8):497–501, July 2017.

[6] T. Mueller and E. Malic. Exciton physics and device application of two-dimensional transition metal dichalcogenide semiconductors. *npj 2D Materials and Applications*, 2(1), September 2018.

[7] X. Zheng and X. Zhang. Excitons in two-dimensional materials. In *Advances in Condensed-Matter and Materials Physics - Rudimentary Research to Topical Technology*. IntechOpen, May 2020.

[8] R. H. Ritchie. Plasma losses by fast electrons in thin films. *Physical Review*, 106(5):874–881, June 1957.

[9] A. A. Rifat, R. Ahmed, A. K. Yetisen, H. Butt, A. Sabouri, G. A. Mahdiraji, S. H. Yun, and F.R. M. Adikan. Photonic crystal fiber based plasmonic sensors. *Sensors and Actuators B: Chemical*, 243:311–325, May 2017.

[10] L. Martín-Moreno and F. J. García-Vidal. Basics of nanoplasmonics. In *World Scientific Handbook of Metamaterials and Plasmonics*, pages 1–19. World Scientific, October 2017.

[11] T. W. Ebbesen, H. J. Lezec, H. F. Ghaemi, T. Thio, and P. A. Wolff. Extraordinary optical transmission through sub-wavelength hole arrays. *Nature*, 391(6668):667–669, February 1998.

[12] F. de León-Pérez, G. Brucoli, F. J. García-Vidal, and L. Martín-Moreno. Theory on the scattering of light and surface plasmon polaritons by arrays of holes and dimples in a metal film. *New Journal of Physics*, 10(10):105017, October 2008.

[13] L. Martín-Moreno and F. J. García-Vidal. Minimal model for optical transmission through holey metal films. *Journal of Physics: Condensed Matter*, 20(30):304214, July 2008.

[14] F. J. Garcia-Vidal, L. Martin-Moreno, T. W. Ebbesen, and L. Kuipers. Light passing through subwavelength apertures. *Reviews of Modern Physics*, 82(1):729–787, March 2010.

[15] S. G. Rodrigo, F. de Leon-Perez, and L. Martin-Moreno. Extraordinary optical transmission: Fundamentals and applications. *Proceedings of the IEEE*, 104(12):2288–2306, December 2016.

[16] M. V. Berry. Quantal phase factors accompanying adiabatic changes. *Proceedings of the Royal Society of London. A. Mathematical and Physical Sciences*, 392(1802):45–57, March 1984.

[17] O.A. Pankratov, S.V. Pakhomov, and B.A. Volkov. Supersymmetry in heterojunctions: Band-inverting contact on the basis of pb1-xsnxte and hg1-xcdxte. *Solid State Communications*, 61(2):93–96, January 1987.

[18] M. Konig, S. Wiedmann, C. Brune, A. Roth, H. Buhmann, L. W. Molenkamp, X.-L. Qi, and S.-C. Zhang. Quantum spin hall insulator state in hgte quantum wells. *Science*, 318(5851):766–770, November 2007.

[19] B. A. Bernevig. *Topological Insulators and Topological Superconductors*. Princeton University Press, December 2013.

[20] K. Y. Bliokh, Y. Gorodetski, V. Kleiner, and E. Hasman. Coriolis effect in optics: Unified geometric phase and spin-hall effect. *Physical Review Letters*, 101(3), July 2008.

[21] T. Chervy, S. Azzini, E. Lorchat, S. Wang, Y. Gorodetski, J. A. Hutchison, S. Berciaud, T. W. Ebbesen, and C. Genet. Room temperature chiral coupling of valley excitons with spin-momentum locked surface plasmons. *ACS Photonics*, 5(4):1281–1287, January 2018.

[22] HL. Liu, CC. Shen, SH. Su, CL. Hsu, MY. Li, and LJ. Li. Optical properties of monolayer transition metal dichalcogenides probed by spectroscopic ellipsometry. *Applied Physics Letters*, 105(20):201905, November 2014.

[23] J. Jackson. *Classical electrodynamics*. Wiley, New York, 1999.

[24] N. W. Ashcroft and N. Mermin. *Solid state physics*. Holt, Rinehart and Winston, New York, 1976.

[25] A. Vial, AS. Grimault, D. Macías, D. Barchiesi, and M. L. de la Chapelle. Improved analytical fit of gold dispersion: application to the modeling of extinction spectra with a finite-difference time-domain method. *Physical Review B*, 71(8), February 2005.

[26] J. Bravo-Abad. Transmisión resonante de luz a través de láminas metálicas nanoestructuradas, October 2006.

[27] M. Beruete, M. Sorolla, I. Campillo, J. S. Dolado, L. Martín-Moreno, J. Bravo-Abad, and F. J. García-Vidal. Enhanced millimeter-wave transmission through subwavelength hole arrays. *Optics Letters*, 29(21):2500, November 2004.

[28] H. Raether. Surface plasmons on smooth surfaces. In *Springer Tracts in Modern Physics*, pages 4–39. Springer Berlin Heidelberg, 1988.

[29] A. Y. Nikitin. Graphene plasmonics. In *World Scientific Handbook of Metamaterials and Plasmonics*, pages 307–338. World Scientific, October 2017.

A Obtainment of the equations

A.1 PEC with holes

Here, we will discuss the procedure to obtain the equations which govern our system. Between the regions I and II (at $z = 0$) we have a 2D film, whereas the medium III consists on a metallic slab with filled-by-dielectric holes (or dimples, depending on the considered system). Every region is dielectric except III, which is metallic and dielectric. The system that we will study is shown in the Fig. 24. The interface between the regions II and III is presented in the Fig. 25, where we can see an example of holes distribution in the metal. There is something that we must clarify: in this App. A.1 we will explain how to obtain the equations in a general way and then, we will consider the specific remarks which differ from the other sections (see App. A.2, App. A.3 and App. A.4). Consequently, the particular features of the other cases will be considered in their respective sections.

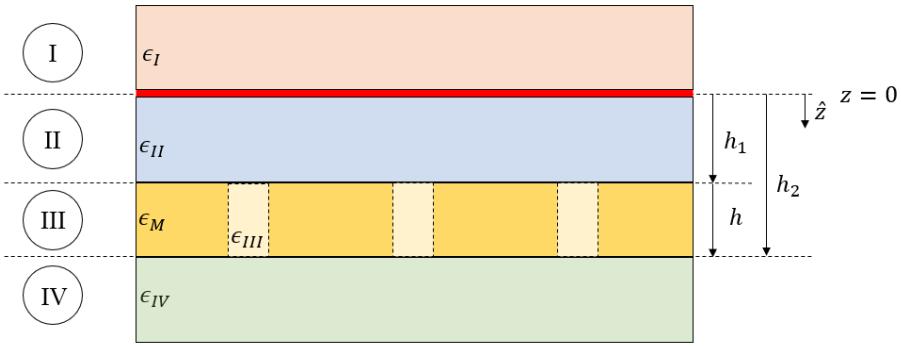

Fig. 24: Scheme of the system that we will study.

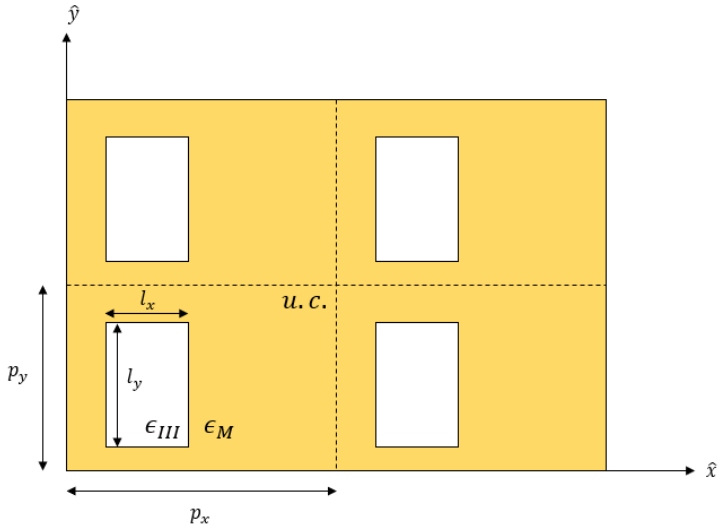

Fig. 25: x-y plane of our system. The discontinuous lines indicate the limits of the unit cell.

Throughout our work we are going to use the coupled-mode method, which consists on formulating the EM fields as a superposition of plane waves with different amplitudes in each region of the space. In this way, we could compute the value of the EM fields everywhere.

In the Fig. 25 we use the term "unit cell" because we will consider that our system is infinitely periodic with this structure as basic module. Also, we will only consider the stationary solutions

for the Maxwell equations, thereby the temporal dependence of the EM fields will be removed along the section. Another remark is that we only need to know the EM fields components which are parallel to the x-y plane, so when we refer to this vectors they are two-components vectors. The z-component of them could be obtained by the Maxwell equations which involve divergences.

Now, focused in this section, we will study our system with holes (i.e. we have a dielectric material crossing the metallic slab from the region II to the IV) and considering that our metal is a PEC (perfect electric conductor, which means that the dielectric constant is $\epsilon_M = -\infty$). The relevance of both conditions will arise when we did the fields matching.

The situation is the following: we have a incident plane wave characterised by an incident momentum ($\vec{k}^0 = (k_x^0, k_y^0)^T$) and an incident polarization (σ^0), and it scatters with our system producing other plane waves with different momenta and polarizations. We will use the Dirac notation so if we project onto the real space we can write:

$$\langle \vec{r}_\parallel | \vec{k}_\parallel, p \rangle = (k_x, k_y)^T \frac{e^{i\vec{k}_\parallel \cdot \vec{r}_\parallel}}{k_\parallel \sqrt{p_x p_y}}, \tag{17}$$

$$\langle \vec{r}_\parallel | \vec{k}_\parallel, s \rangle = (-k_y, k_x)^T \frac{e^{i\vec{k}_\parallel \cdot \vec{r}_\parallel}}{k_\parallel \sqrt{p_x p_y}}, \tag{18}$$

where $\vec{k}_\parallel = (k_x, k_y)^T$, $\vec{r}_\parallel = (x_\parallel, y_\parallel)^T$, $k_\parallel = \sqrt{k_x^2 + k_y^2}$ and, p and s are values for the polarization σ. Note that the vectorial character of the previous expressions is determined by the polarization. When $\vec{k}_\parallel = \vec{0}$ the distinction between the case $\sigma = p$ and the case $\sigma = s$ becomes arbitrary, so we take wilfully that $\langle \vec{r}_\parallel | \vec{0}, p \rangle = (1,0)^T / \sqrt{p_x p_y}$ and $\langle \vec{r}_\parallel | \vec{0}, s \rangle = (0,1)^T / \sqrt{p_x p_y}$.

As EM fields we will take the electric field ($\vec{E}_i$) but instead of the magnetic field ($\vec{H}_i$) we will use the quantity: $-\hat{u}_z \times \vec{H}_i$, which is:

$$|-\hat{u}_z \times \vec{H}_i\rangle = \pm Y^i_{\vec{k}_\parallel, \sigma} \, |\vec{E}_i\rangle \,, \tag{19}$$

where $\hat{u}_z$ is the unit vector in the z-direction, i refers to the different regions ($i = I, II, III, IV$), the $\pm$ depends on if the the wave is going in the z-direction or in the opposite, respectively, and $Y^i_{\vec{k}_\parallel, \sigma}$ is the admittance of the i-th region for the $\vec{k}_\parallel$ momentum and the σ polarization. These can be:

$$Y^i_{\vec{k}_\parallel, p} = \frac{\epsilon_i g}{k_z^i}, \tag{20}$$

$$Y^i_{\vec{k}_\parallel, s} = \frac{k_z^i}{g}, \tag{21}$$

where $g = \omega/c = 2\pi/\lambda$ and $k_z^i = \sqrt{\epsilon_i g^2 - k_\parallel^2}$. And here, the values of $\vec{k}_\parallel$ depend on the region that we are considering. If we are at I, II or IV then

$$\vec{k}_\parallel = (k_x, k_y)^T = (k_x^0 + G_x, k_y^0 + G_y)^T, \tag{22}$$

where $\vec{G} = (G_x, G_y)^T = 2\pi \left(\frac{m_x}{p_x}, \frac{m_y}{p_y} \right)^T$ is a vector of the reciprocal lattice. There m_x and m_y are: $m_x = \{-M_x, -M_x + 1, \ldots, M_x - 1, M_x\} \in \mathbb{Z}$ and $m_y = \{-M_y, -M_y + 1, \ldots, M_y - 1, M_y\} \in \mathbb{Z}$, being M_x and M_y the number of Bragg's waves that we will consider. And if we are at the region III then

$$\vec{k}_\parallel = (k_x, k_y)^T = \pi \left(\frac{n_x}{l_x}, \frac{n_y}{l_y} \right)^T, \tag{23}$$

but we will only consider $n_x = 0$ and $n_y = 1$, which is the less energy mode for the hole. Then, the fundamental waveguide mode is:

$$\langle \vec{r}_\parallel | n \rangle = (1,0)^T \sqrt{\frac{2}{l_x l_y}} \sin(q_y(y + l_y/2)) \quad \text{for } \vec{r}_\parallel \text{ inside the hole and 0 otherwise,} \tag{24}$$

where n only refers to we are considering the n-th hole, but the modes for every hole are the same.

Before writing the fields for all the regions we want to explain the notation we will use for the plane waves modes and for the holes modes. For us:

$$|0\rangle = |\vec{k}^0, \sigma^0\rangle\,, \tag{25}$$

$$|G\rangle = |\vec{k}^0 + \vec{G}, \sigma\rangle \tag{26}$$

and

$$|n\rangle = |n\text{-th hole}\rangle\,, \tag{27}$$

but for $|n\rangle$ we must clarify that these modes have no defined polarization so we arbitrarily choose $Y_n^{III} = k_z^{III}/g$ as the modal admittance of the n-th hole. Both, $|G\rangle$ and $|n\rangle$, constitute two orthonormal basis.

Thereby, the EM fields of the different regions are:

$$\begin{aligned} |\vec{E}_I(z)\rangle &= |0\rangle\, e^{ik_z^I(k^0)z} + \sum_G r_G\, |G\rangle\, e^{-ik_z^I(G)z}, \\ |-\hat{u}_z \times \vec{H}_I(z)\rangle &= Y_0^I\, |0\rangle\, e^{ik_z^I(k^0)z} - \sum_G Y_G^I r_G\, |G\rangle\, e^{-ik_z^I(G)z}, \end{aligned} \tag{28}$$

$$\begin{aligned} |\vec{E}_{II}(z)\rangle &= \sum_G \tau_G\, |G\rangle\, e^{ik_z^{II}(G)z} + \sum_G \rho_G\, |G\rangle\, e^{-ik_z^{II}(G)z}, \\ |-\hat{u}_z \times \vec{H}_{II}(z)\rangle &= \sum_G Y_G^{II} \tau_G\, |G\rangle\, e^{ik_z^{II}(G)z} - \sum_G Y_G^{II} \rho_G\, |G\rangle\, e^{-ik_z^{II}(G)z}, \end{aligned} \tag{29}$$

$$\begin{aligned} |\vec{E}_{III}(z)\rangle &= \sum_n A_n\, |n\rangle\, e^{ik_z^{III}(n)(z-h_1)} + \sum_n B_n\, |n\rangle\, e^{-ik_z^{III}(n)(z-h_1)}, \\ |-\hat{u}_z \times \vec{H}_{III}(z)\rangle &= \sum_n Y_n^{III} A_n\, |n\rangle\, e^{ik_z^{III}(n)(z-h_1)} - \sum_n Y_n^{III} B_n\, |n\rangle\, e^{-ik_z^{III}(n)(z-h_1)}, \end{aligned} \tag{30}$$

$$\begin{aligned} |\vec{E}_{IV}(z)\rangle &= \sum_G t_G\, |G\rangle\, e^{ik_z^{IV}(G)(z-h_2)}, \\ |-\hat{u}_z \times \vec{H}_{IV}(z)\rangle &= \sum_G Y_G^{IV} t_G\, |G\rangle\, e^{ik_z^{IV}(G)(z-h_2)}, \end{aligned} \tag{31}$$

where $\{r_G,\ \tau_G,\ \rho_G,\ A_n,\ B_n\ t_G\}$ are the parameters that we will obtain through the matching of EM fields at the interface between different regions. In other words, via requiring the continuity of fields at the interfaces. We want to clarify here that when we are summing over G, we are summing over the reciprocal lattice vectors and the polarizations.

As a picture is worth a thousand words, we will show in the Fig. 26 what all these parameters mean.

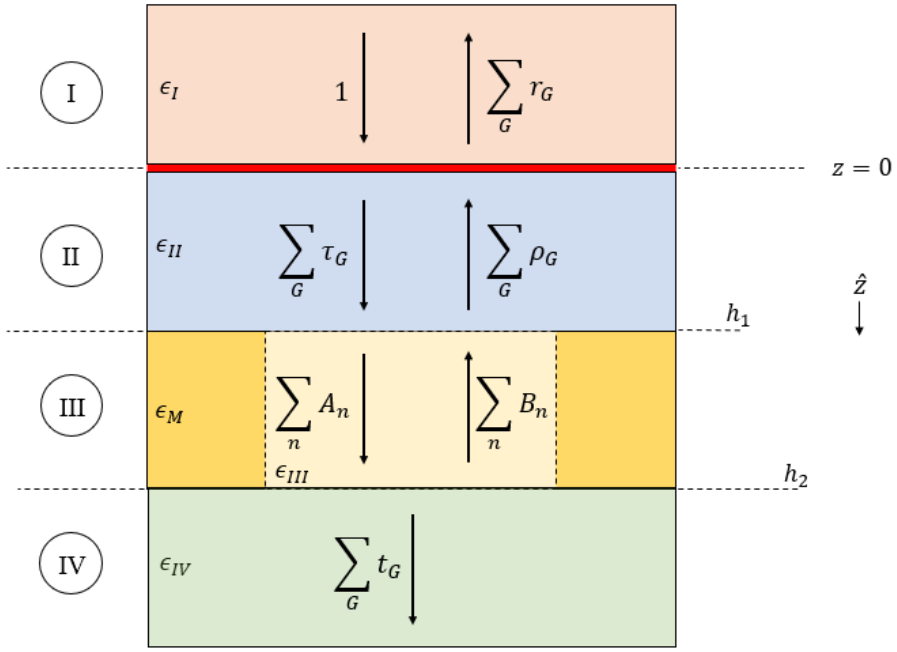

Fig. 26: In this representation it is shown the physical meaning of each parameter that appears in the definition of the fields in the different regions (see Eqs. 28, 29, 30 and 31).

Knowing this, let's start with the interface between regions I and II, i.e. at $z = 0$.

- Continuity of electric field (parallel-to-the-plane-$z = 0$ components):

$$|0\rangle + \sum_G r_G |G\rangle = \sum_G \tau_G |G\rangle + \sum_G \rho_G |G\rangle , \tag{32}$$

and projecting onto $|G\rangle$:

$$\delta_{G,0} + r_G = \tau_G + \rho_G, \tag{33}$$

because of orthonormality of the basis vectors.

- The magnetic field has a discontinuity characterised by the 2D film conductivity placed at $z = 0$, so-called σ_{2D}. However, due to the using of the Gauss convention we will take the following variable $\alpha = 2\pi\sigma_{2D}/c$. So, the equation we must satisfy is:

$$|-\hat{u}_z \times \vec{H}_{II}(z = 0)\rangle - |-\hat{u}_z \times \vec{H}_I(z = 0)\rangle = -2\alpha |\vec{E}_{II}(z = 0)\rangle . \tag{34}$$

Thus,

$$\sum_G Y_G^{II} \tau_G |G\rangle - \sum_G Y_G^{II} \rho_G |G\rangle - Y_0^I |0\rangle + \sum_G Y_G^I r_G |G\rangle = -2\alpha \left(\sum_G \tau_G |G\rangle + \sum_G \rho_G |G\rangle \right), \tag{35}$$

and projecting again onto $|G\rangle$:

$$Y_G^{II}(\tau_G - \rho_G) - Y_0^I \delta_{G,0} + Y_G^I r_G = -2\alpha (\tau_G + \rho_G) . \tag{36}$$

Now, if we look at the interface between regions II and III, i.e. at $z = h_1$:

- Continuity of electric field:

$$\sum_G \tau_G |G\rangle e^{ik_z^{II}(G)h_1} + \sum_G \rho_G |G\rangle e^{-ik_z^{II}(G)h_1} = \sum_n A_n |n\rangle + \sum_n B_n |n\rangle , \tag{37}$$

and projecting onto $|G\rangle$, considering from now that $e^{ik_z^{II}(G)h_1} = e_G$ and defining the overlapping integral that we discuss in App. B as $S_{G,n} = \langle G|n\rangle$:

$$\tau_G e_G + \rho_G e_G^{-1} = \sum_n A_n S_{G,n} + \sum_n B_n S_{G,n} \tag{38}$$

- The magnetic field is continuous where there is no metal, i.e., in the surface of the hole (dielectric):

$$\sum_G Y_G^{II} \tau_G |G\rangle e_G - \sum_G Y_G^{II} \rho_G |G\rangle e_G^{-1} = \sum_n Y_n^{III} A_n |n\rangle - \sum_n Y_n^{III} B_n |n\rangle , \tag{39}$$

but here we project onto $|n\rangle$ because it is on the hole where this continuity is satisfied. Thus,

$$\sum_G Y_G^{II} \tau_G e_G S_{G,n}^* - \sum_G Y_G^{II} \rho_G e_G^{-1} S_{G,n}^* = Y_n^{III} A_n - Y_n^{III} B_n. \tag{40}$$

And the last interface corresponds to the regions III and IV, i.e., at $z = h_2$:

- Continuity of electric field:

$$\sum_n A_n |n\rangle e^{ik_z^{III}(n)h} + \sum_n B_n |n\rangle e^{-ik_z^{III}(n)h} = \sum_G t_G |G\rangle , \tag{41}$$

and, projecting onto $|G\rangle$ and considering from now that $e^{ik_z^{III}(n)h} = e_n$ we obtain that,

$$\sum_n A_n e_n S_{G,n} + \sum_n B_n e_n^{-1} S_{G,n} = t_G. \tag{42}$$

- Again, the magnetic field at $z = h_2$ is only continuous on the hole, thus:

$$\sum_n Y_n^{III} A_n |n\rangle e_n - \sum_n Y_n^{III} B_n |n\rangle e_n^{-1} = \sum_G Y_G^{IV} t_G |G\rangle , \tag{43}$$

and projecting onto $|n\rangle$,

$$Y_n^{III} A_n e_n - Y_n^{III} B_n e_n^{-1} = \sum_G Y_G^{IV} t_G S_{G,n}^*. \tag{44}$$

In short, we want to know 6 parameters and we have 6 equations in order to look for them (see Eqs. 33, 36, 38, 40, 42 and 44). Although we really have more than 6 parameters and 6 equations because we have as pairs of $\{A_n,\ B_n\}$ as considered holes, and the same happens with the parameters which depend on G.

The necessary calculations to obtaining the final equations are a bit tedious so we will omit them. However, we will explain the main steps in order to achieve our equations. Firstly, we will isolate the r_G from the Eq. 33 and replace it in the Eq. 36. From here, we can take τ_G as a function of ρ_G and introduce it in the Eqs. 38 and 40. Then, we isolate ρ_G as a function of $\{A_n\}$ and $\{B_n\}$ from one of these two equations and reintroduce it into the other one. In this way, we have obtained an equation which relates $\{A_n\}$ and $\{B_n\}$. Now, we can isolate t_G from the Eq. 42 as a function of $\{A_n\}$ and $\{B_n\}$ and replace it into the Eq. 44, obtaining then other equation which uniquely depends on $\{A_n\}$ and $\{B_n\}$. So, we are able to compute every parameter if we solve the system of equations for $\{A_n\}$ and $\{B_n\}$. Nevertheless, instead of using as parameters $\{A_n\}$ and $\{B_n\}$ we will use other pair of parameters called modal amplitudes $\{E_n, E_n'\}$, which

correspond to the modal amplitudes of the electric field in the illuminated and no-illuminated surfaces of each hole ($z = h_1$ and $z = h_2$ interfaces), respectively. They are defined as

$$\begin{aligned} E_n &= A_n + B_n, \\ E'_n &= -(A_n e_n + B_n e_n^{-1}), \end{aligned} \tag{45}$$

where the negative sign in the second one comes from the fact that the normal vector which is pointing to the hole has contrary sign to $\hat{u}_z$. Then, after substituting these parameters in the equations we are ready to write the final equation such as:

$$\boxed{\begin{aligned} &(G_{nn}^{I,II} - \Sigma_n)E_n + \sum_{m\neq n} G_{nm}^{I,II} E_m - G_n^V E'_n = I_{0,n}^{ex} \\ &(G_{nn}^{IV} - \Sigma_n)E'_n + \sum_{m\neq n} G_{nm}^{IV} E_m - G_n^V E_n = 0 \end{aligned}} \tag{46}$$

where it is seen that there are a lot of terms that we have not talked about. They depend on the admitances, on the overlapping integrals, on the exponentials and on the 2D film conductivity. The shapes of these terms are expressed here below, in the Eqs. 47, 48, 49, 50 and 51.

$$G_{nm}^{I,II} = \sum_G iY_G^{II} \frac{(Y_G^{II} + Y_G^I + 2\alpha) + e_G^2(Y_G^{II} - Y_G^I + 2\alpha)}{(Y_G^{II} + Y_G^I + 2\alpha) - e_G^2(Y_G^{II} - Y_G^I + 2\alpha)} S_{G,n}^* S_{G,m}, \tag{47}$$

$$G_{nm}^{IV} = \sum_G iY_G^{IV} S_{G,n}^* S_{G,m}, \tag{48}$$

$$I_{0,n}^{ex} = i \frac{4Y_0^I Y_0^{II} S_{0,n}^* e_{G=0}}{(Y_0^{II} + Y_0^I + 2\alpha) - e_{G=0}^2(Y_0^{II} - Y_0^I + 2\alpha)}, \tag{49}$$

$$G_n^V = iY_n^{III} \frac{2e_n^{-1}}{1 - e_n^{-2}}, \tag{50}$$

$$\Sigma_n = iY_n^{III} \frac{1 + e_n^{-2}}{1 - e_n^{-2}}. \tag{51}$$

The physical relevance of these terms can be well-understood if we observe the Fig. 27.

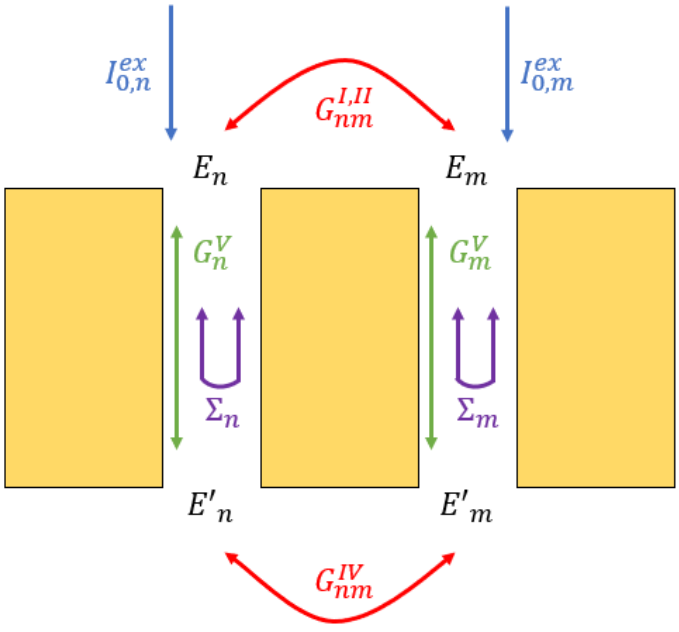

Fig. 27: Physical relevance of the terms that appear in the equations for the parameters of our set-up.

Here we present a little explanation about them. $G^{I,II}_{nm}$ and G^{IV}_{nm} correspond to the coupling between n-th and m-th apertures throughout any propagating or evanescent modes at the $z = h_1$ and $z = h_2$ surfaces, respectively. $I^{ex}_{0,n}$ is the external illumination, basically governed by the coupling between the incident plane wave (indicated by 0) and the waveguide mode corresponding to the n-th entry aperture. G^{V}_{n} represents the coupling between the $z = h_1$ and $z = h_2$ interfaces but for the same hole (n-th). Obviously this term only appears if we are considering holes, for dimples there is no exit aperture. Finally, Σ_n is related to the bouncing when the EM fields inside n-th hole reach the end of the waveguide.

A.2 PEC with dimples

In this section we will focus in the system which has dimples instead of holes (i.e. we have metallic slab dented and these dents are filled with a dielectric material) and considering that our metal is a PEC (perfect electric conductor, which means that the dielectric constant is $\epsilon_M = -\infty$). Again, these both conditions will affect to the fields-matching conditions. Obviously, in this case the region IV does not exist. In Fig. 28 we show an scheme of this system.

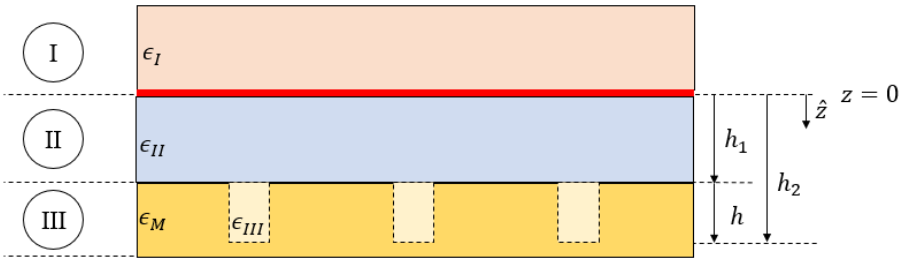

Fig. 28: The system that we will study in this section: dimples.

As we say above, the region IV does not exist because the dielectric does not totally cross the entire metallic slab. Nevertheless, this system still has a lot of similarities with the system studied in the App. A.1. Clearly the expressions of the EM fields in the regions I, II and III have the same form (see Eqs. 28, 29 and 30). And in the same way we have already obtained the matching conditions at the interfaces: $z = 0$ and $z = h_1$ (see Eqs. 33, 36, 38 and 40) because there is no difference for these interfaces in this situation. Here we need to remark that now h is the dimples depth.

Then, the last matching condition we need is the cancellation of the fields at $z = h_2$. So,

$$\sum_n A_n e_n \left|n\right\rangle + \sum_n B_n e_n^{-1} \left|n\right\rangle = 0, \tag{52}$$

from we infer the last condition:

$$A_n e_n + B_n e_n^{-1} = 0. \tag{53}$$

Here it is convenient to recall the expression which relates A_n's and B_n's as result of solving the Eqs. 33, 36, 38 and 40. This is,

$$iY^{III}_n (A_n - B_n) - I^{ex}_{0,n} = -\sum_m G^{I,II}_{nm} (A_m + B_m), \tag{54}$$

and defining again the modal amplitude as

$$E_n = A_n + B_n \tag{55}$$

we can obtain the final equation via some calculations. Thereby,

$$\boxed{(G_{nn}^{I,II} - \Sigma_n)E_n + \sum_{m\neq n} G_{nm}^{I,II} E_m = I_{0,n}^{ex}} \tag{56}$$

The terms which appears in the final expression have the same form as before:

$$G_{nm}^{I,II} = \sum_G iY_G^{II} \frac{(Y_G^{II} + Y_G^I + 2\alpha) + e_G^2(Y_G^{II} - Y_G^I + 2\alpha)}{(Y_G^{II} + Y_G^I + 2\alpha) - e_G^2(Y_G^{II} - Y_G^I + 2\alpha)} S_{G,n}^* S_{G,m}, \tag{57}$$

$$I_{0,n}^{ex} = i\frac{4Y_0^I Y_0^{II} S_{0,n}^* e_{G=0}}{(Y_0^{II} + Y_0^I + 2\alpha) - e_{G=0}^2(Y_0^{II} - Y_0^I + 2\alpha)}, \tag{58}$$

$$\Sigma_n = iY_n^{III}\frac{1 + e_n^{-2}}{1 - e_n^{-2}}. \tag{59}$$

And clearly $G_{nm}^{IV} = 0$ and $G_n^V = 0$ because there is no region IV and there is no coupling then between the entry and the "exit" of the dimples.

A.3 SIBC with holes

In this section we will try to implement a new level of complexity, and thus, of reality, to our metallic slab. So far we had considered the PEC (Perfect Electric Conductor) approximation but from now on we will consider the so-called SIBC approximation. It means "Surface Impedance Boundary Conditions". This can be understood as a first-order Taylor expansion in $z_s = 1/\sqrt{\epsilon_M(\lambda) + 1}$. On the other hand, the PEC approximation constitutes the zero-order Taylor expansion because for the PEC, $\epsilon_M = -\infty$ and then $z_s = 0$. This z_s is used to relate the tangential components of the electric and magnetic fields at the surface of the metal such as

$$|\vec{E}\rangle = z_s\,|\vec{H} \times \hat{u}_n\rangle\,, \tag{60}$$

where $\hat{u}_n$ is an unitary vector orthogonal to the surface and that points to the inside of the material.

There is also other aspect provided by the SIBC approximation: the enlarging of the holes size. Since the metal is no more a perfect conductor, the EM fields penetrate the material and we do not have the condition of cancelling the fields at the surface. Therefore, this can be seen as an effective enlarging of the holes because we are not considering the SIBC approximation for the vertical surfaces, only for horizontal ones. We will model it by the use of the skin depth, defined as

$$\delta = \frac{\lambda \cdot Im(z_s)}{2\pi}, \tag{61}$$

and we will use it as an addition to the holes length and width but corrected by a phenomenologically estimated parameter, i.e.

$$l' = l + a\delta, \tag{62}$$

being $a \simeq 1.25$ for our case [26].

We have already explained the novelties of the SIBC respect PEC so we are ready to present the calculation of the final equations. Again, the expressions for the EM fields in each region is the same that we presented in Eqs. 28, 29, 30 and 31. Besides, the matching conditions for the first interface ($z = 0$) are the same because nothing changes there (see Eqs. 33 and 36). However, at the second and third interfaces ($z = h_1$ and $z = h_2$ respectively) the conditions do

change. Instead of requiring the continuity of the electric and magnetic fields as we did before, we will require the continuity of a new field (F) defined below in Eq. 63, and also the continuity of the magnetic field. This new field is:

$$|\vec{F}\rangle = |\vec{E}\rangle - z_s\,|\vec{H}\times\hat{u}_n\rangle = |\vec{E}\rangle - z_s\,|-\hat{u}_n\times\vec{H}\rangle\,. \tag{63}$$

Here it is important to remark one point: $\vec{F}$ is continuous at the interface but in both metal and dielectric (hole). It is continuous at the dielectric surface because both electric and magnetic fields are continuous independently. And it is also continuous at the metal surface because of Eq. 60. This is why we will project onto the plane waves modes when we work with the $|\vec{F}\rangle$ continuity. And since the continuity of $|\vec{H}\rangle$ is only satisfied in the holes, we will project onto the holes modes when we work with the $|\vec{H}\rangle$ (this is only continuous in the holes).

So, if we attend to the interface between regions II and III, i.e. at $z = h_1$:

- Continuity of field F, considering that $\hat{u}_n = \hat{u}_z$,

$$\sum_G(\tau_G e_G+\rho_G e_G^{-1})\,|G\rangle - z_s\sum_G Y_G^{II}(\tau_G e_G-\rho_G e_G^{-1})\,|G\rangle = \sum_n(A_n+B_n)\,|n\rangle - z_s\sum_n Y_n^{III}(A_n n B_n)\,|n\rangle\,, \tag{64}$$

  where projecting onto $|G\rangle$ and recalling the definition of the overlapping integrals we obtain, after some reorders, that

$$\tau_G e_G(1-z_sY_G^{II}) + \rho_G e_G^{-1}(1+z_sY_G^{II}) = \sum_n S_{G,n}(A_n(1-z_sY_n^{III}) + B_n(1+z_sY_n^{III})). \tag{65}$$

  Here we define three quantities that we will use right now and a bit later: $f_n^{\pm} = 1\pm z_sY_n^{III}$, $f_G^{\pm} = 1\pm z_sY_G^{II}$ and $f_G^{'\pm} = 1\pm z_sY_G^{IV}$. So, having this in mind we can rewrite the previous condition as

$$\tau_G e_G f_G^- + \rho_G e_G^{-1} f_G^+ = \sum_n S_{G,n}(A_n f_n^- + B_n f_n^+) \tag{66}$$

- Continuity of magnetic field in the hole, so the derived equation is the Eq. 40.

Now, we look at the interface between regions III and IV, i.e. at $z = h_2$:

- Continuity of field F, taking into account that $\hat{u}_n = -\hat{u}_z$,

$$\sum_n(A_n e_n + B_n e_n^{-1})\,|n\rangle + z_s\sum_n Y_n^{III}(A_n e_n - B_n e_n^{-1})\,|n\rangle = \sum_G t_G\,|G\rangle + z_s\sum_G Y_G^{IV}t_G\,|G\rangle\,, \tag{67}$$

  projecting onto $|G\rangle$ and making use of the previous definitions we can directly write

$$\sum_n S_{G,n}(A_n e_n f_n^+ + B_n e_n^{-1} f_n^-) = t_G f_G^{'+} \tag{68}$$

- Continuity of magnetic field in the hole, so the derived equation is the Eq. 44.

Now, we have to solve the six equations that we have (see Eqs. 33, 36, 66, 40, 68 and 44). For that purpose, we will use a similar procedure to the used in App. A.1. However, in this case we have to put the modal amplitudes ($\{E_n,\ E'_n\}$) as a function of the modal parameters ($\{A_n,\ B_n\}$) in other way such as:

$$\begin{aligned} E_n &= A_n f_n^- + B_n f_n^+, \\ E'_n &= -(A_n e_n f_n^+ + B_n e_n^{-1} f_n^-). \end{aligned} \tag{69}$$

Then, the equations governing our system are:

$$\boxed{\begin{aligned}&(G^{I,II}_{nn}-\Sigma_n)E_n+\sum_{m\neq n}G^{I,II}_{nm}E_m-G^{V}_{n}E'_n=I^{ex}_{0,n}\\&(G^{IV}_{nn}-\Sigma_n)E'_n+\sum_{m\neq n}G^{IV}_{nm}E_m-G^{V}_{n}E_n=0,\end{aligned}} \tag{70}$$

where the different terms have the following shapes,

$$G^{I,II}_{nm}=\sum_G iY^{II}_G\frac{(Y^{II}_G+Y^{I}_G+2\alpha)+e^2_G(Y^{II}_G-Y^{I}_G+2\alpha)}{f^{+}_G(Y^{II}_G+Y^{I}_G+2\alpha)-e^2_G f^{-}_G(Y^{II}_G-Y^{I}_G+2\alpha)}S^*_{G,n}S_{G,m}, \tag{71}$$

$$G^{IV}_{nm}=\sum_G i\frac{Y^{IV}_G}{f'^{+}_G}S^*_{G,n}S_{G,m}, \tag{72}$$

$$I^{ex}_{0,n}=i\frac{4Y^{I}_0Y^{II}_0S^*_{0,n}e_{G=0}}{f^{+}_{G=0}(Y^{II}_0+Y^{I}_0+2\alpha)-e^2_{G=0}f^{-}_{G=0}(Y^{II}_0-Y^{I}_0+2\alpha)}, \tag{73}$$

$$G^{V}_{n}=iY^{III}_n\frac{2e^{-1}_n}{f^{+2}_n-e^{-2}_nf^{-2}_n}, \tag{74}$$

$$\Sigma_n=iY^{III}_n\frac{f^{+}_n+e^{-2}_nf^{-}_n}{f^{+2}_n-e^{-2}_nf^{-2}_n}. \tag{75}$$

A.4 SIBC with dimples

In this section we will focus again in the system which has dimples instead of holes and we will consider also the SIBC approximation, which means that the dielectric constant is finite and it depends on the wavelength. Again, these both features will affect to the fields-matching conditions. As we said, in this case the region IV does not exist and in the Fig. 28 we can see an scheme of this system. This case is thus a combination of the Apps. A.2 and A.3.

As we say above, the region IV does not exist because the dielectric does not totally cross the entire metallic slab. Obviously the expressions of the EM fields in the regions I, II and III have the same form see (Eqs. 28, 29 and 30). And in the same way we have already obtained the matching conditions at the interfaces: $z=0$ and $z=h_1$ (see Eqs. 33, 36, 66 and 40) because there is no difference for such interfaces in this situation. Here we need to recall that now h is the dimples depth.

Therefore, the last matching condition we need is the cancellation of the fields at $z=h_2$, i.e., at the interface between regions III and IV. For this we will use the cancellation of the field F defined in the Eq. 63. We have to remark that as the metal exists beyond the dimple, thus $\hat{u}_n=\hat{u}_z$. So,

$$\sum_n(A_ne_n+B_ne^{-1}_n)\,|n\rangle-z_s\sum_n Y^{III}_n(A_ne_n-B_ne^{-1}_n)\,|n\rangle=0, \tag{76}$$

from we infer that (using the definition of $f^{\pm}_n$)

$$A_ne_nf^{-}_n+B_ne^{-1}_nf^{+}_n=0. \tag{77}$$

And now, knowing that the modal amplitude is defined such as

$$E_n=A_nf^{-}_n+B_nf^{+}_n, \tag{78}$$

we are ready to write the final equation of this system:

$$\boxed{(G_{nn}^{I,II} - \Sigma_n)E_n + \sum_{m \neq n} G_{nm}^{I,II} E_m = I_{0,n}^{ex}} \tag{79}$$

The terms that appear in this expression can be written as:

$$G_{nm}^{I,II} = \sum_G i Y_G^{II} \frac{(Y_G^{II} + Y_G^I + 2\alpha) + e_G^2(Y_G^{II} - Y_G^I + 2\alpha)}{f_G^+(Y_G^{II} + Y_G^I + 2\alpha) - e_G^2 f_G^-(Y_G^{II} - Y_G^I + 2\alpha)} S_{G,n}^* S_{G,m}, \tag{80}$$

$$I_{0,n}^{ex} = i \frac{4 Y_0^I Y_0^{II} S_{0,n}^* e_{G=0}}{f_{G=0}^+(Y_0^{II} + Y_0^I + 2\alpha) - e_{G=0}^2 f_{G=0}^-(Y_0^{II} - Y_0^I + 2\alpha)}, \tag{81}$$

$$\Sigma_n = i Y_n^{III} \frac{f_n^+ e_n^{-2} + f_n^-}{f_n^+ f_n^-(1 - e_n^{-2})}, \tag{82}$$

and clearly $G_{nm}^{IV} = 0$ and $G_n^V = 0$ because there is no region IV and there is no coupling between the entry and the "exit" of the dimples.

B Calculation of the overlapping integrals

B.1 Simplest case: non-rotated hole

First of all, we will calculate the overlapping integral of the simplest setup, i.e., a non-rotated hole, because this procedure will ease the calculation for the rotated case. This means that the hole orientation angle is $\theta = 0^{\text{o}}$ for this case. So, the configuration that we will discuss here is shown in the Fig. 29, where we can properly observe that the hole is characterised by the position of its centre on the unit cell (x_c, y_c), also by the length of its sides (l_x, l_y) and finally by the angle of orientation (θ), which is 0^{o} in this case and then we do not show it.

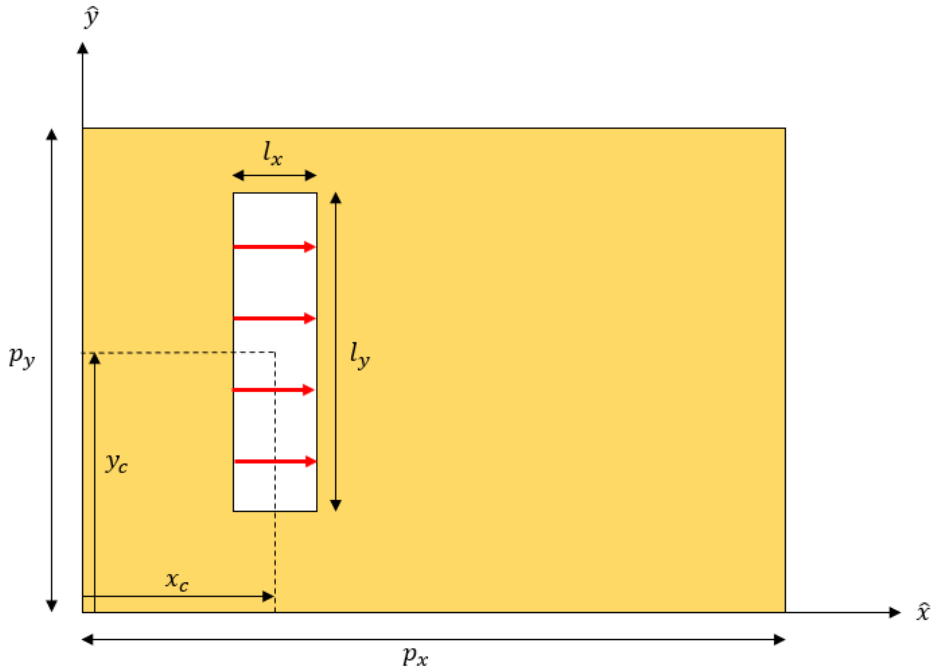

Fig. 29: Representation of the case $\theta = 0$.

As we have already introduced, the overlapping integral that we must calculate is:

$$S_{G,n} = \langle G|n\rangle = \langle \vec{G}, \sigma|n\rangle = \int_{u.c.} \langle \vec{G}, \sigma|\vec{r}_{\parallel}\rangle \langle \vec{r}_{\parallel}|n\rangle \, d\vec{r}_{\parallel}, \tag{83}$$

where "u.c." alludes to that the integration is made over the unit cell $\{x_{\parallel} \in (0, p_x), y_{\parallel} \in (0, p_y)\}$, and here we are going to use $\vec{G} = \vec{k}_{\parallel} = \vec{k}^0 + \vec{G}$.

We had previously seen the explicit functional form of the plane waves as a function their wavevector $(\vec{G})$ and their polarization ($\sigma = s$ or p). Nevertheless, we write again these forms:

$$\langle \vec{r}_{\parallel}|\vec{G}, p\rangle = (k_x, k_y)^T \frac{e^{i\vec{k}_{\parallel}\cdot\vec{r}_{\parallel}}}{k_{\parallel}\sqrt{p_x p_y}}, \tag{84}$$

$$\langle \vec{r}_{\parallel}|\vec{G}, s\rangle = (-k_y, k_x)^T \frac{e^{i\vec{k}_{\parallel}\cdot\vec{r}_{\parallel}}}{k_{\parallel}\sqrt{p_x p_y}}, \tag{85}$$

but when $\vec{G} = \vec{0}$ the distinction between the case $\sigma = p$ and the case $\sigma = s$ is arbitrary, so we take wilfully that $\langle \vec{r}_{\parallel}|\vec{0}, p\rangle = (1, 0)^T/\sqrt{p_x p_y}$ and $\langle \vec{r}_{\parallel}|\vec{0}, s\rangle = (0, 1)^T/\sqrt{p_x p_y}$.

The fundamental waveguide mode of the n-th hole is:

$$\langle \vec{r}_{\parallel}|n\rangle = (1,0)^T \sqrt{\frac{2}{l_x l_y}} \sin(q_y(y+l_y/2)) \quad \text{for } \vec{r}_{\parallel} \text{ inside the hole and 0 otherwise.} \tag{86}$$

Here we write the n-th hole just for generality. However, in this calculations we will only consider one hole (the hole in the Fig. 29).

Regarding these three expressions we must also clarify that k_x and k_y are the components of the $\vec{G}$ considered, $k_{\parallel} = \sqrt{k_x^2 + k_y^2}$, $q_y = \pi/l_y$ and pre-factors are taken to normalize the modes over the unit cell. The direction of the electric field of the fundamental mode is shown as red arrows in the Fig. 29. It is also important to emphasize that since the hole mode is zero out of the latter, we can consider the position vector such as: $\vec{r}_{\parallel} = \vec{r}_c + \vec{r}$, where $\vec{r}_c$ is the vector which leads to the hole centre (x_c, y_c), and $\vec{r} = (x, y)$ is any point of the hole (in the reference framework of the hole: $\{x \in (-l_x/2, l_x/2), y \in (-l_y/2, l_y/2)\}$).

Taking all these details in consideration we can rewrite the Eq. 83 as:

$$S_{G,n} = \int_{hole} \langle \vec{G}, \sigma|\vec{r}_c + \vec{r}\rangle \langle \vec{r}|n\rangle \, d\vec{r} = \int_{hole} f_{\vec{G},\sigma} \frac{e^{-i\vec{k}_{\parallel}\cdot(\vec{r}_c+\vec{r})}}{\sqrt{p_x p_y}} \sqrt{\frac{2}{l_x l_y}} \sin(q_y(y+l_y/2)) d\vec{r}, \tag{87}$$

where $f_{\vec{G},\sigma}$ is the outcome of the scalar product of the bi-vector of each mode. In other words:

$$f_{\vec{G},p} = \frac{1}{k_{\parallel}}(k_x, k_y) \cdot (1,0)^T = k_x/k_{\parallel}, \tag{88}$$

and

$$f_{\vec{G},s} = \frac{1}{k_{\parallel}}(-k_y, k_x) \cdot (1,0)^T = -k_y/k_{\parallel}, \tag{89}$$

Now, we are going to define a constant (C) which allows us to lighten the notation, this is:

$$C = \sqrt{\frac{2}{p_x p_y l_x l_y}} f_{\vec{G},\sigma}. \tag{90}$$

Still on the overlapping integral:

$$\begin{aligned}
S_{G,n} &= C \int_{hole} e^{-i\vec{k}_{\parallel}\cdot(\vec{r}_c+\vec{r})} \sin(q_y(y+l_y/2)) d\vec{r} \\
&= C e^{-i(k_x x_c + k_y y_c)} \int_{-l_x/2}^{l_x/2} e^{-ik_x x} dx \int_{-l_y/2}^{l_y/2} e^{-ik_y y} \sin(q_y(y+l_y/2)) dy \\
&= C e^{-i(k_x x_c + k_y y_c)} \cdot \frac{e^{-ik_x x}}{-ik_x}\Big|_{-l_x/2}^{l_x/2} \cdot \int_{-l_y/2}^{l_y/2} e^{-ik_y y} \frac{e^{iq_y(y+l_y/2)} - e^{-iq_y(y+l_y/2)}}{2i} dy \\
&= \frac{C}{2i} e^{-i(k_x x_c + k_y y_c)} \cdot \frac{2\sin(k_x l_x/2)}{k_x} \cdot \int_{-l_y/2}^{l_y/2} e^{-ik_y y}(ie^{iq_y y} + ie^{-iq_y y}) dy \\
&= \frac{C}{2} e^{-i(k_x x_c + k_y y_c)} l_x \cdot \mathrm{sinc}(k_x l_x/2) \cdot \left(\frac{e^{-i(k_y - q_y)y}}{-i(k_y - q_y)} + \frac{e^{-i(k_y + q_y)y}}{-i(k_y + q_y)} \right)\Bigg|_{-l_y/2}^{l_y/2} \\
&= \frac{C}{2} e^{-i(k_x x_c + k_y y_c)} l_x \cdot \mathrm{sinc}(k_x l_x/2) \cdot l_y \cdot (\mathrm{sinc}((k_y - q_y)l_y/2) + \mathrm{sinc}((k_y + q_y)l_y/2)) \\
&= \sqrt{\frac{l_x l_y}{2 p_x p_y}} f_{\vec{G},\sigma} e^{-i(k_x x_c + k_y y_c)} \cdot \mathrm{sinc}(k_x l_x/2) \cdot (\mathrm{sinc}((k_y - q_y)l_y/2) + \mathrm{sinc}((k_y + q_y)l_y/2)).
\end{aligned} \tag{91}$$

In the step from the third line to the fourth we have used that $q_y = \pi/l_y$ and thus $e^{\pm i q_y l_y/2} = \pm i$. A second comment is that sinc() corresponds to the cardinal sine function.

Just to emphasize the result:

$$\boxed{S_{G,n} = \sqrt{\frac{l_x l_y}{2p_x p_y}} f_{\vec{G},\sigma} e^{-i(k_x x_c + k_y y_c)} \cdot \mathrm{sinc}(k_x l_x/2) \cdot (\mathrm{sinc}((k_y - q_y) l_y/2) + \mathrm{sinc}((k_y + q_y) l_y/2))} \tag{92}$$

So, this Eq. 92 is the expression for the overlapping integral of the EM modes (plane waves with hole modes) in a non-rotated hole. As we have already said, the information about the plane waves is enclosed in $G = (\vec{G} = (k_x, k_y), \sigma)$ whereas the information about the hole is enclosed in n, which determines the centre is at (x_c, y_c) and the side lengths are (l_x, l_y).

Now it is time to promote to a more general case: a rotated hole. In this way, we will be able to propose a wider variety of holes configurations. This is going to be presented in the next section (see App. **??**).

B.2 General case: rotated hole

Here we will discuss the case which θ takes an arbitrary value. This configuration is shown in the Fig. 30.

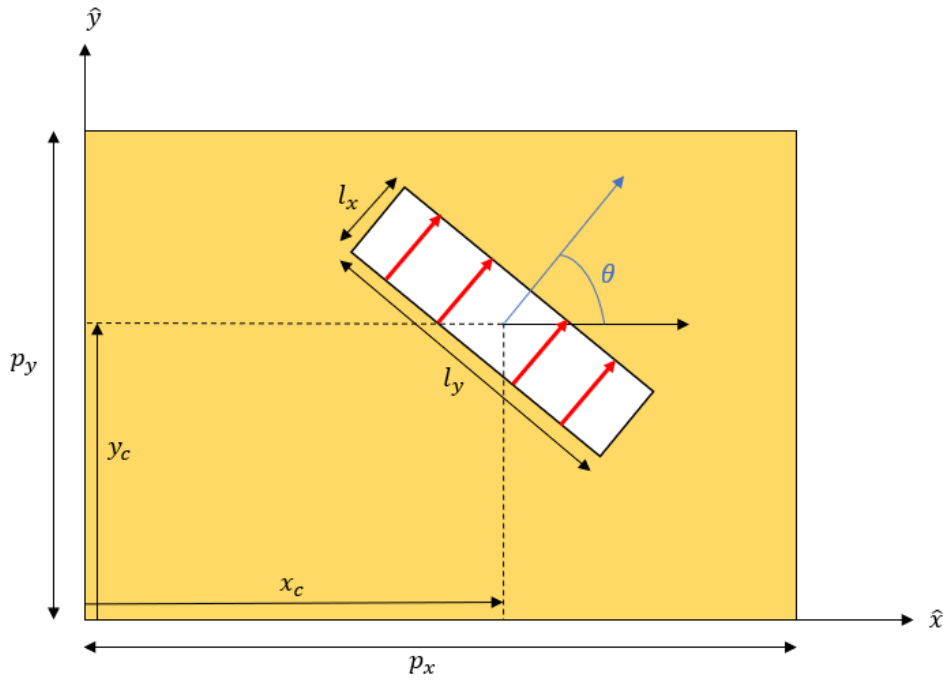

Fig. 30: Representation of the case arbitrary θ.

Obviously, the overlapping integral that we have to solve is the same that the previous one, with the difference of having other integration limits. The explicit functional form of the plane waves takes exactly the same form as before. In contrast, the hole mode is different because of the angle rotation. However, this can be solved by a shift (θ) in the reference framework. In this manner, we can recover the form of the hole mode of the $\theta = 0^o$ case but in the (x', y')

framework. This rotation of the axes is shown in the Fig. 31

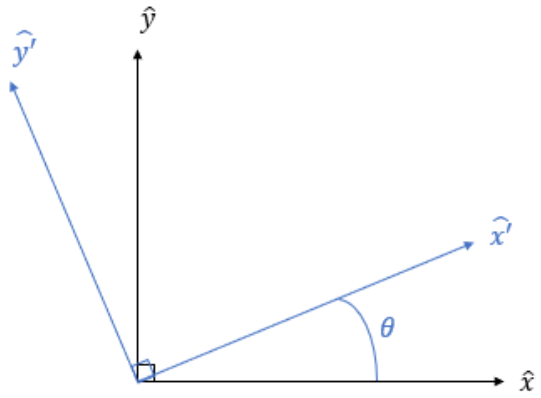

Fig. 31: Representation of the axes rotation. From (x, y) framework to (x', y') framework shifted an angle θ.

Hence:

$$\langle \vec{r}_{\parallel} | n \rangle = (1,0)'^{T} \sqrt{\frac{2}{l_x l_y}} \sin\big(q_y(y' + l_y/2)\big) \quad \text{for } \vec{r}_{\parallel} \text{ inside the hole and 0 otherwise.} \tag{93}$$

Note that the prime in $(0,1)'^{T}$ is also important, it takes this form in the primed reference framework.

Here, it is convenient to state how the coordinates are defined in both reference frameworks as a function of the other one. Thus:

$$\begin{pmatrix} x' \\ y' \end{pmatrix} = \begin{pmatrix} \cos\theta & \sin\theta \\ -\sin\theta & \cos\theta \end{pmatrix} \begin{pmatrix} x \\ y \end{pmatrix}, \qquad \begin{pmatrix} x \\ y \end{pmatrix} = \begin{pmatrix} \cos\theta & -\sin\theta \\ \sin\theta & \cos\theta \end{pmatrix} \begin{pmatrix} x' \\ y' \end{pmatrix}, \tag{94}$$

where we assign $R(\theta)$ to the matrix which, given (x, y), returns (x', y'); and $R^{-1}(\theta)$ to the matrix which performs the opposite transformation.

Before solving the overlapping integral, it is convenient to compute the scalar product between the bi-vectors of both modes. For that purpose, we will need to write the hole bi-vector in the basis of the plane waves modes using $R^{-1}(\theta)$, in order to have both in the same basis and thus, be able to calculate it.

The expression for the constant C is:

$$C = \sqrt{\frac{2}{p_x p_y l_x l_y}} f_{\vec{G},\sigma}, \tag{95}$$

but $f_{\vec{G},\sigma}$ is different because the bi-vectors have to live in the same basis:

$$f_{\vec{G},p} = \frac{1}{k_{\parallel}}(k_x, k_y) \cdot \begin{pmatrix} \cos\theta & -\sin\theta \\ \sin\theta & \cos\theta \end{pmatrix} \cdot (1,0)'^{T} = \frac{1}{k_{\parallel}}(k_x, k_y) \cdot (\cos\theta, \sin\theta)^{T} = (k_x \cos\theta + k_y \sin\theta)/k_{\parallel}, \tag{96}$$

and

$$f_{\vec{G},s} = \frac{1}{k_\parallel}(-k_y, k_x)\cdot(\cos\theta, \sin\theta)^T = (-k_y\cos\theta + k_x\sin\theta)/k_\parallel. \tag{97}$$

Taking this into account, the overlapping integral is:

$$\begin{aligned} S_{G,n} &= \int_{u.c.} \langle \vec{G}, \sigma|\vec{r}_\parallel\rangle \langle \vec{r}_\parallel|n\rangle \, d\vec{r}_\parallel = C\int_{hole} e^{-i\vec{k}_\parallel\cdot\vec{r}_\parallel}\sin\big(q_y(y'+l_y/2)\big)dxdy \\ &= Ce^{-i(k_x x_c + k_y y_c)}\int_{hole} e^{-i\vec{k}_\parallel\cdot\vec{r}}\sin\big(q_y(y'+l_y/2)\big)dxdy \end{aligned} \tag{98}$$

Since the integration limits are easier to be written in the primed reference framework, we will perform a change of variables to these (x', y'). For this purpose, we will use that $\vec{r} = R^{-1}(\theta)\vec{r}'$ and that the Jacobian is 1 ($dxdy = dx'dy'$). Then:

$$S_{G,n} = Ce^{-i(k_x x_c + k_y y_c)}\int_{hola} e^{-i\vec{k}_\parallel\cdot R^{-1}(\theta)\cdot\vec{r}'}\sin\big(q_y(y'+l_y/2)\big)dx'dy'. \tag{99}$$

So, we can integrate over the primed coordinates if we define $\vec{k}'_\parallel$:

$$\vec{k}'_\parallel = \vec{k}_\parallel R^{-1}(\theta) = (k_x, k_y)\begin{pmatrix}\cos\theta & -\sin\theta \\ \sin\theta & \cos\theta\end{pmatrix} = (k_x\cos\theta + k_y\sin\theta, -k_x\sin\theta + k_y\cos\theta). \tag{100}$$

Thereby, we obtain an integral with an alike shape such as the first case one, whose resolution is presented here:

$$\begin{aligned} S_{G,n} &= Ce^{-i(k_x x_c + k_y y_c)}\int_{hole} e^{-i\vec{k}'_\parallel\cdot\vec{r}'}\sin\big(q_y(y'+l_y/2)\big)dx'dy'. \\ &= Ce^{-i(k_x x_c + k_y y_c)}\int_{-l_x/2}^{l_x/2} e^{-ik'_x x'}dx'\int_{-l_y/2}^{l_y/2} e^{-ik'_y y'}\sin\big(q_y(y'+l_y/2)\big)dy' \\ &= \sqrt{\frac{l_x l_y}{2p_x p_y}} f_{\vec{G},\sigma} e^{-i(k_x x_c + k_y y_c)}\cdot\mathrm{sinc}(k'_x l_x/2)\cdot(\mathrm{sinc}((k'_y - q_y)l_y/2) + \mathrm{sinc}((k'_y + q_y)l_y/2)). \end{aligned} \tag{101}$$

Note that in this case $f_{\vec{G},\sigma}$ depends on θ, as well as $\vec{k}'_\parallel$. Now, if we take $\theta = 0$ both recover the expressions presented in App. **??**.

Again, just to emphasize the result:

$$\boxed{S_{G,n} = \sqrt{\frac{l_x l_y}{2p_x p_y}} f_{\vec{G},\sigma} e^{-i(k_x x_c + k_y y_c)}\cdot\mathrm{sinc}(k'_x l_x/2)\cdot(\mathrm{sinc}((k'_y - q_y)l_y/2) + \mathrm{sinc}((k'_y + q_y)l_y/2))} \tag{102}$$

So, this Eq. 102 is the expression for the overlapping integral of the EM modes in an arbitrarily-rotated hole.

C Calculation of the energy fluxes

C.1 PEC with holes

In this section we will discuss the general procedure to obtain the energy fluxes for each region of the space and then, we will particularize for each specific situation. The general system for which we will figure out the EM fluxes is presented in a previous appendix (App. A.1) or in Fig. 32.

The calculation of these EM fluxes enables us to study different interesting quantities as the transmittance or reflectance of the system, or the absorbance of the 2D film and metallic slab. Therefore, this estimation is crucial for achieving results.

First of all, we need to know the time-averaged EM energy flux per unit time passing through our system. This is described by the Poynting vector $\vec{S}(\vec{r}, z)$, where $\vec{r}$ corresponds to the coordinates which are on the parallel plane to the 2D film, i.e., $\vec{r} = (x, y)^T$. The expression for the Poynting vector is shown in the Eq. 103 below,

$$\vec{S}(\vec{r}, z) = \frac{1}{2}\left(\vec{E}(\vec{r}, z) \times \vec{H}(\vec{r}, z)^*\right), \tag{103}$$

where the factor $1/2$ comes from the time average of $\vec{S}(\vec{r}, z, t)$.

Since we are really interested in the flux that crosses every region of our system, we need to define four horizontal planes where we will compute these fluxes. These planes are: $P_1 := (z = 0^-)$, $P_2 := (z = 0^+)$, $P_3 := (z = h_1^+)$ and $P_4 := (z = h_2^+)$. P_1, P_2 and P_4 are infinite planes whereas P_3 takes only the section of the hole/dimple. Here, we can say that P_1 is replaceable by any horizontal plane with $z < 0$ because the region I is dielectric and thus, there is no change in its flux. This reasoning can be similarly applied to the other defined planes. We just do it in this way looking for notation simplicity. This is shown in the Fig. 32.

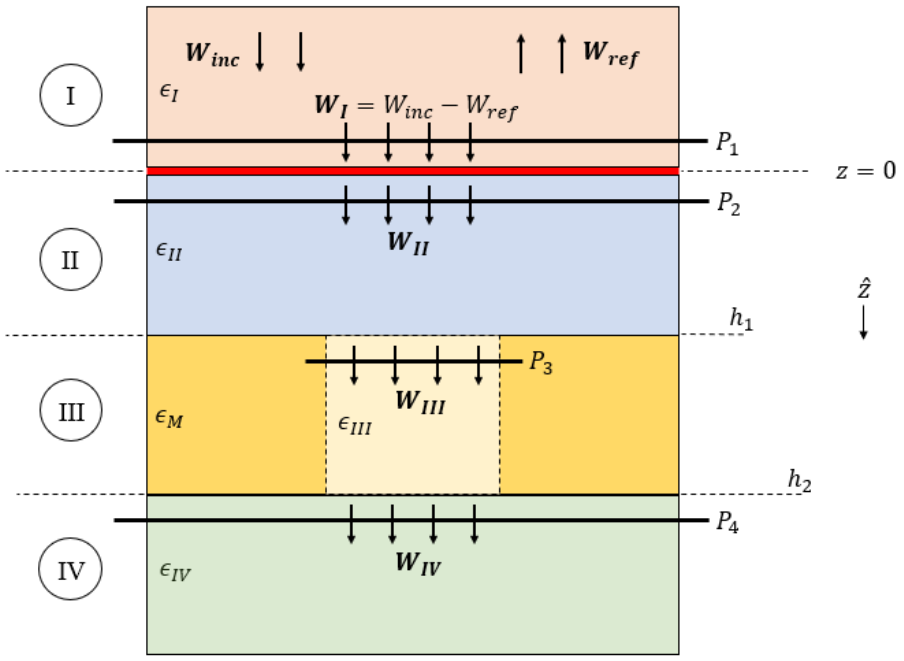

Fig. 32: Scheme of our system. Here we can see the four regions, the four horizontal planes and the direction of the z-axis. We can also see the different energy fluxes of interest, as well as the definition of W_I: the subtraction of the reflective flux from the incident flux.

So, the EM energy flux crossing one of the planes, let's say P_i, can be computed following the Eq. 104.

$$W_i = \int_{P_i} d\vec{r}\, Re[\hat{u}_z \cdot \vec{S}(\vec{r}, z_i)] = \int_{P_i} d\vec{r}\, Re\left[\hat{u}_z \cdot \frac{1}{2}\left(\vec{E}_i(\vec{r}, z_i) \times \vec{H}_i(\vec{r}, z_i)^*\right)\right], \tag{104}$$

where i refers to both the regions (I, II, III, IV) and the planes $(1, 2, 3, 4)$, because there is concordance between them. And z_i refers to the value of the z coordinate which defines the i-th plane. This EM energy flux can be rewritten such as

$$W_i = \frac{1}{2}\int_{P_i} d\vec{r}\, Re\left[\langle -\hat{u}_z \times \vec{H}_i(\vec{r}, z_i) | \vec{E}_i(\vec{r}, z_i)\rangle\right], \tag{105}$$

using the properties of the scalar and vectorial products, as well as the chosen notation in App. A.1. It is also important to remark that from now on we will drop the factor $1/2$ because we will normalize every flux by the incident flux W_{inc}, which contains the same factor too.

Now, taking into account this Eq. 105 and the modal expansions of the electric and magnetic fields presented in App. A.1 (see Eqs. 28, 29, 30 and 31), we are ready to compute each EM energy flux.

We can start considering P_1 and thus, computing W_I,

$$\begin{aligned} W_I &= \int_{P_1} d\vec{r}\, Re\left[\langle -\hat{u}_z \times \vec{H}_I(\vec{r}, 0^-) | \vec{E}_I(\vec{r}, 0^-)\rangle\right] \\ &= \int_{P_1} d\vec{r}\, Re\left[\left(Y_0^{I*}\langle 0| - \sum_G Y_G^{I*} r_G^* \langle G|\right) \cdot \left(|0\rangle + \sum_G r_G |G\rangle\right)\right] \\ &= Re\left[Y_0^{I*} - Y_0^{I*}(r_0^* - r_0) - \sum_G Y_G^{I*}|r_G|^2\right], \end{aligned} \tag{106}$$

where we have used the property of orthonormality of the plane waves, i.e.,

$$\int_{P_1} d\vec{r}\, \langle G|G'\rangle = \delta_{G,G'}, \tag{107}$$

being the $\delta_{G,G'}$ the Kronecker delta ($|G\rangle$'s are the only terms which depends on $\vec{r}$).

However, since we will only consider that the incident illumination is propagating ($k_z^I(0) = \sqrt{\epsilon_I(\omega/c)^2 - (k_x^0)^2 - (k_y^0)^2} \in \mathbb{R}$) and thus not evanescent, the term $Re[Y_0^{I*}(r_0^* - r_0)] = 0$. This is because if the incident fields are propagating, then Y_0^{I*} is real, but as $(r_0^* - r_0)$ is imaginary, then the product is imaginary too and as a consequence of this, the real part of it is zero. So, the energy flux for the first plane is

$$W_I = Re\left[Y_0^{I*} - \sum_G Y_G^{I*}|r_G|^2\right]. \tag{108}$$

The first term corresponds to the incident flux $W_{inc} = Re\left[Y_0^{I*}\right]$ whereas the second belongs to the scattering of the incident beam with the surface, i.e., $W_{ref} = Re\left[\sum_G Y_G^{I*}|r_G|^2\right]$. Therefore, as we had already presented in Fig. 32, $W_I = W_{inc} - W_{ref}$. We are going to keep the previous expressions in this way but when we will plot these quantities we will normalize by the incident flux W_{inc} as we already said. We can also observe from the expression for W_{ref} that only the propagating modes will play a part in the reflection. It is also important to emphasize

here that when we say 0 or G we really refer to $(\vec{k}^0, \sigma^0)$ and $(\vec{k}^0 + \vec{G}, \sigma = s, p)$, respectively.

Now, we could think about how to write $\{r_G\}$ in terms of $\{E_n, E'_n\}$, because these are the parameters that we derive from the final equations presented in App. A. However, these $\{E_n, E'_n\}$ depend on the considered system (PEC with holes, PEC with dimples, ...) so firstly we will obtain the other EM fluxes and after, we will particularize for each case.

Then, we consider the second plane, P_2, and compute W_{II},

$$\begin{aligned} W_{II} =& \int_{P_2} d\vec{r}\, Re\left[\langle -\hat{u}_z \times \vec{H}_{II}(\vec{r}, 0^+) | \vec{E}_{II}(\vec{r}, 0^+)\rangle\right] \\ =& \int_{P_2} d\vec{r}\, Re\left[\left(\sum_G Y_G^{II*}(\tau_G^* - \rho_G^*)\langle G|\right) \cdot \left(\sum_G (\tau_G + \rho_G)|G\rangle\right)\right] \\ =& Re\left[\sum_G Y_G^{II*}(|\tau_G|^2 - |\rho_G|^2 + \tau_G^*\rho_G - \tau_G\rho_G^*)\right]. \end{aligned} \tag{109}$$

Despite of the subtraction of the two last terms is imaginary, we must keep all the contributions because Y_G^{II*} may be evanescent or propagating in the region II. So, if the mode in this region is propagating, only the first two terms will contribute to W_{II}, whereas if it is evanescent the contributions to W_{II} will only come from the last two terms.

We can keep up with the third plane, P_3, and compute then W_{III},

$$\begin{aligned} W_{III} =& \int_{P_3} d\vec{r}\, Re\left[\langle -\hat{u}_z \times \vec{H}_{III}(\vec{r}, h_1^+) | \vec{E}_{III}(\vec{r}, h_1^+)\rangle\right] \\ =& \int_{P_3} d\vec{r}\, Re\left[\left(\sum_n Y_n^{III*}(A_n^* - B_n^*)\langle n|\right) \cdot \left(\sum_n (A_n + B_n)|n\rangle\right)\right] \\ =& Re\left[\sum_n Y_n^{III*}(|A_n|^2 - |B_n|^2 + A_n^*B_n - A_nB_n^*)\right]. \end{aligned} \tag{110}$$

In this case, we use the same argument as before to preserve all terms.

We are therefore left with the calculation of W_{IV}. So, taking the fourth plane, P_4,

$$\begin{aligned} W_{IV} =& \int_{P_4} d\vec{r}\, Re\left[\langle -\hat{u}_z \times \vec{H}_{IV}(\vec{r}, h_2^+) | \vec{E}_{IV}(\vec{r}, h_2^+)\rangle\right] \\ =& \int_{P_4} d\vec{r}\, Re\left[\left(\sum_G Y_G^{IV*} t_G^* \langle G|\right) \cdot \left(\sum_G t_G |G\rangle\right)\right] \\ =& Re\left[\sum_G Y_G^{IV*}|t_G|^2\right]. \end{aligned} \tag{111}$$

Just as reminder, we want to say again that we will normalize every flux by the incident. In this way, there are some interesting quantities we can compute. For example, the transmittance is defined as

$$T = \frac{W_{IV}}{W_{inc}} = \frac{Re\left[\sum_G Y_G^{IV*}|t_G|^2\right]}{Re\left[Y_0^{I*}\right]}, \tag{112}$$

or the reflectance,

$$R = \frac{W_{ref}}{W_{inc}} = \frac{Re\left[\sum_G Y_G^{I*}|r_G|^2\right]}{Re\left[Y_0^{I*}\right]}. \tag{113}$$

So, we have the expressions for every energy flux as a function of $\{r_G, \tau_G, \rho_G, A_n, B_n, t_G\}$. Throughout the calculations we made in App. A, we are able to write each parameter in terms of the modal amplitudes $\{E_n, E'_n\}$, but they depend also on the situation that we consider: it is not the same A_n for holes or for dimples, or even for PEC or SIBC. Thus, we have the expressions for the fluxes, which are fixed in terms of the parameters, but the parameters does change depending on the case

As a consequence, this is the point where we particularize to having holes crossing our metal and considering it such as a PEC. Using the Eqs. 33, 36, 38 and 40 we can write $\{\rho_G, \tau_G, r_G\}$ as a function of $\{E_n\}$ in the following way,

$$\rho_G = \frac{Y_G^I + Y_G^{II} + 2\alpha}{(Y_G^I + Y_G^{II} + 2\alpha) - e_G^2(Y_G^I - Y_G^{II} + 2\alpha)} \cdot \left(e_G \sum_n S_{G,n} E_n - \frac{2Y_G^I e_G^2}{Y_G^I + Y_G^{II} + 2\alpha} \delta_{G,0} \right), \quad (114)$$

$$\tau_G = \frac{2Y_G^I \delta_{G,0} - \rho_G(Y_G^I - Y_G^{II} + 2\alpha)}{Y_G^I + Y_G^{II} + 2\alpha}, \quad (115)$$

and

$$r_G = -\delta_{G,0} + \tau_G + \rho_G. \quad (116)$$

In order to obtain $\{A_n, B_n\}$ as a function of $\{E_n, E'_n\}$ we just need to attend to the definitions of these last ones, done in Eq. 45. Therewith,

$$A_n = -e_n^{-1} \cdot \frac{e_n^{-1} E_n + E'_n}{1 - e_n^{-2}}, \quad (117)$$

and

$$B_n = \frac{E_n + e_n^{-1} E'_n}{1 - e_n^{-2}}. \quad (118)$$

To conclude, from the definition of $\{E'_n\}$ and taking the Eq. 42 we deduce

$$t_G = -\sum_n S_{G,n} E'_n. \quad (119)$$

As may be seen, the computation of the EM energy fluxes for "PEC with holes" is concluded since we have obtained the expressions of these fluxes and the parameters. We have recalled App. A in almost every point because it is there where we did a deeper analysis of the equations and, thus, of the parameters. We must clarify that some shortenings used above are well-justified in App. A.1 and we have passed over them because of this.

C.2 PEC with dimples

In this case, we will deal with a PEC again but considering dimples instead of holes. In other words, now we do not cross completely the metallic slab but we keep metal under our perforation. We can see a representation of this system in Fig. 33.

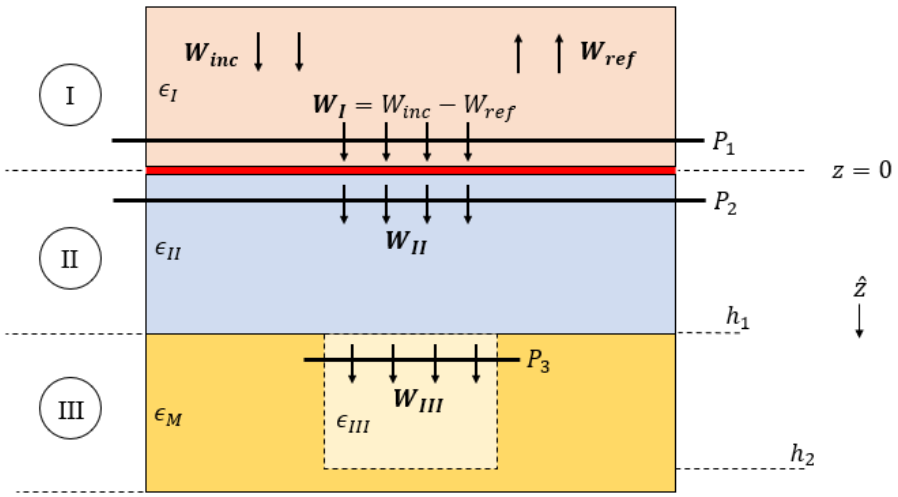

Fig. 33: Scheme of our system. Here we can see the three regions, the three horizontal planes and the direction of the z-axis. We can also see the different energy fluxes of interest.

Now, the results for this system will be easier to obtain because we will use the previous section outcome. As we observed from App. A.2, the fourth region does not exist, which means that $\{E'_n = 0\}$, $W_{IV} = 0$ and $\{t_G = 0\}$. On the other hand, the system that we have just presented is the same as before until the third region, which has changed. This allows us to write straightforward some of the desired parameters:

$$\rho_G = \frac{Y_G^I + Y_G^{II} + 2\alpha}{(Y_G^I + Y_G^{II} + 2\alpha) - e_G^2(Y_G^I - Y_G^{II} + 2\alpha)} \cdot \left(e_G \sum_n S_{G,n} E_n - \frac{2Y_G^I e_G^2}{Y_G^I + Y_G^{II} + 2\alpha} \delta_{G,0} \right), \quad (120)$$

$$\tau_G = \frac{2Y_G^I \delta_{G,0} - \rho_G(Y_G^I - Y_G^{II} + 2\alpha)}{Y_G^I + Y_G^{II} + 2\alpha}, \quad (121)$$

and

$$r_G = -\delta_{G,0} + \tau_G + \rho_G, \quad (122)$$

which are exactly the same as in the system "PEC with holes" (see App. C.1). It may be also derived from the continuity of the fields, posed in the App. A, as we did in the previous section (see App. C.1). Then, we only need to compute the expressions for $\{A_n, B_n\}$ as a function of $\{E_n\}$ in order to complete the description of this situation. For this purpose, we will consider the definition of E_n and the condition that the fields go to zero at $z = h_2$, i.e.,

$$\begin{aligned} E_n &= A_n + B_n, \\ 0 &= A_n e_n + B_n e_n^{-1}, \end{aligned} \quad (123)$$

expressions which have already been used in App. A.2. From these, we can write the last two parameters such as

$$A_n = -\frac{e_n^{-2} E_n}{1 - e_n^{-2}}, \quad (124)$$

and

$$B_n = \frac{E_n}{1 - e_n^{-2}}. \quad (125)$$

Therefore, since we have finally written the expressions of the "five" parameters as a function of the modal amplitude $\{E_n\}$, and the shape of the fluxes is the same as we wrote in the Sec. C.1, we have just completed the characterisation of the EM energy fluxes for this system: "PEC with dimples".

C.3 SIBC with holes

In this case, we will deal with a metal satisfying the SIBC (Surface Impedance Boundary Conditions) approximation, but we will take again the situation of having holes crossing entirely the metallic slab. Since the only thing changing respect of App. C.1 is the corresponding metal approximation, the scheme which represents this system is also shown in Fig. 32.

Obviously, in this case we have to obtain the expressions for all parameters because we have to infer the four EM fluxes. However, the equations from we infer these expressions are different. They are included in Ap. A.3. It is clear that the continuity of the fields for the interface between regions I and II is unchanged, but for the interfaces at $z = h_1$ and $z = h_2$ the situation is different because we considered the continuity of the $(\vec{F} = \vec{E} - z_s\vec{H} \times \hat{u}_n)$ field. So, from Eqs. 33, 36, 66, 40, 68 and 44, we can derive the wanted parameters.

$$\rho_G = \frac{-2Y_G^I e_G f_G^- \delta_{G,0} + (Y_G^I + Y_G^{II} + 2\alpha)\sum_n S_{G,n}E_n}{e_G^{-1} f_G^+ (Y_G^I + Y_G^{II} + 2\alpha) - e_G f_G^- (Y_G^I - Y_G^{II} + 2\alpha)}, \tag{126}$$

$$\tau_G = \frac{2Y_G^I \delta_{G,0} - \rho_G (Y_G^I - Y_G^{II} + 2\alpha)}{Y_G^I + Y_G^{II} + 2\alpha}, \tag{127}$$

and

$$r_G = -\delta_{G,0} + \tau_G + \rho_G, \tag{128}$$

where e_G's and $f_G^{\pm}$'s had already been defined in App. A. Apparently the expressions for $\{\tau_G, r_G\}$ are the same as before but not indeed because $\{\rho_G\}$ have been modified by the $f_G^{\pm}$'s.

Following the procedure used in App. C.1, in order to obtain the expression for $\{t_G\}$ we must take the continuity equation for the $\vec{F}$ field at the third interface (see Eq. 68) and the definition of E'_n, which is

$$E'_n = -(A_n f_n^+ e_n + B_n f_n^- e_n^{-1}). \tag{129}$$

Combining them we get

$$t_G = \frac{-1}{f_G'^+} \sum_n S_{G,n} E'_n. \tag{130}$$

Finally, the way of obtaining the last two parameters $\{A_n, B_n\}$ is through the definition of $\{E_n, E'_n\}$. E'_n is written just above and E_n is

$$E_n = A_n f_n^- + B_n f_n^+. \tag{131}$$

So, solving from these two equations the required parameters:

$$A_n = -\frac{E_n e_n^{-2} f_n^- + E'_n e_n^{-1} f_n^+}{\left(f_n^+\right)^2 - e_n^{-2}\left(f_n^-\right)^2}, \tag{132}$$

and

$$B_n = \frac{E_n f_n^+ + E'_n f_n^- e_n^{-1}}{\left(f_n^+\right)^2 - e_n^{-2}\left(f_n^-\right)^2}. \tag{133}$$

C.4 SIBC with dimples

Now, we will deal with a metal satisfying the SIBC approximation again. We will consider the situation of having holes not crossing entirely the metallic slab, i.e., having dimples. Since the only thing changing respect of App. C.2 is the corresponding metal approximation, the scheme which represents this system is also shown in Fig. 33.

The results for this system will be easier to obtain because we will use the previous section outcome. The fourth region does not exist, which means that $\{E'_n = 0\}$, $W_{IV} = 0$ and $\{t_G = 0\}$. On the other hand, the system that we have just presented is the same as the previous until the third region, which has changed. This allows us to write straightforward some of the desired parameters:

$$\rho_G = \frac{-2Y_G^I e_G f_G^- \delta_{G,0} + (Y_G^I + Y_G^{II} + 2\alpha)\sum_n S_{G,n} E_n}{e_G^{-1} f_G^+ (Y_G^I + Y_G^{II} + 2\alpha) - e_G f_G^- (Y_G^I - Y_G^{II} + 2\alpha)}, \tag{134}$$

$$\tau_G = \frac{2Y_G^I \delta_{G,0} - \rho_G (Y_G^I - Y_G^{II} + 2\alpha)}{Y_G^I + Y_G^{II} + 2\alpha}, \tag{135}$$

and

$$r_G = -\delta_{G,0} + \tau_G + \rho_G, \tag{136}$$

having the same shape as in App. C.3.

By contrast, reaching the expressions for $\{A_n, B_n\}$ is not so immediate because we have to combine the definition of $\{E_n\}$, which is shown at Eq. 131, and the fact that the $\vec{F}$ field goes to zero at $z = h_2$. This has already been discussed in App. A.4, where we just have to consider that $\hat{u}_n = \hat{u}_z$ because they are dimples rather than holes. The corresponding condition is

$$A_n e_n f_n^- + B_n e_n^{-1} f_n^+ = 0. \tag{137}$$

So, combining both we are able to express $\{A_n, B_n\}$ such as

$$A_n = \frac{-E_n e_n^{-2}}{f_n^- (1 - e_n^{-2})}, \tag{138}$$

and

$$B_n = \frac{E_n}{f_n^+ (1 - e_n^{-2})}. \tag{139}$$

Then, we have established the expressions for every required parameter, thus ending the analysis of the EM energy fluxes in all four considered different systems.

D Absorption spectrum of a 2D film

In this section we intend to obtain the expression for the 2D film absorption. A representation of the system we want to solve is shown in Fig. 34.

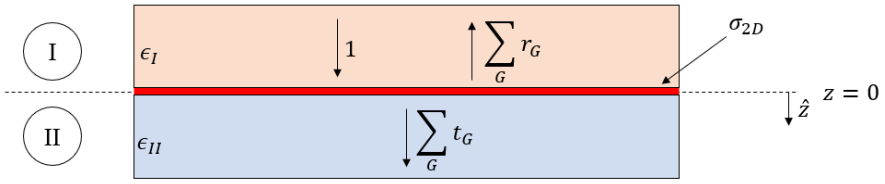

Fig. 34: Scheme of our system in the most general way. We can observe both regions separated by the 2D film and the parameters characterising each medium. It can also be seen the ($z = 0$)-plane and the 2D film attribute, σ_{2D}.

As we can deduce from the utilisation of summations in the Fig. 34, we will make use of the modal expansion method in order to tackle the problem. Basically, the situation consists on two regions with arbitrary dielectric constant each one and separated by a 2D layer. This 2D layer has atomic width. Here it is important to remark that we will not use this σ_{2D} conductivity for our calculations but α, which is just a convenient redefinition:

$$\alpha = \frac{2\pi\sigma_{2D}}{c}. \tag{140}$$

So, what happens is this: we have an incident plane wave coming to the 2D layer and defined by its incident momentum and polarization. This plane wave scatters against the film and a portion is reflected and other is transmitted, characterised by r_0 and t_0 respectively. The portion that is not either reflected or transmitted, is absorbed.

The procedure that we will follow is equivalent to the used in App. A. Firstly, we will pose the expressions of the EM fields for both region I and region II. Then, we will require the satisfaction of the boundary conditions for the parallel electric and magnetic fields. And to conclude, we will compute the 2D film absorption by the calculation of the EM energy fluxes in both regions.

Thereby, the EM fields expressions are written as:

$$\begin{aligned} |\vec{E}_I(z)\rangle &= |0\rangle\, e^{ik_z^I(k_0)z} + \sum_G r_G\, |G\rangle\, e^{-ik_z^I(G)z}, \\ |-\hat{u}_z \times \vec{H}_I(z)\rangle &= Y_0^I\, |0\rangle\, e^{ik_z^I(k_0)z} - \sum_G Y_G^I r_G\, |G\rangle\, e^{-ik_z^I(G)z}, \end{aligned} \tag{141}$$

for the first region, and

$$\begin{aligned} |\vec{E}_{II}(z)\rangle &= \sum_G t_G\, |G\rangle\, e^{ik_z^{II}(G)z}, \\ |-\hat{u}_z \times \vec{H}_{II}(z)\rangle &= \sum_G Y_G^{II} t_G\, |G\rangle\, e^{ik_z^{II}(G)z}, \end{aligned} \tag{142}$$

for the second.

Every element that we have written above is well-justified in App. A, but just as reminder we can say that for example $|G\rangle$ correspond to the different modes that we consider, or Y_G^i is the modal admitance for the i-th region with momentum $\vec{k}^0 + \vec{G}$ and polarization σ. Note that

the use of Dirac's notation is just for convenience and, as we have said, can be fully understood if you recall App. A.

The next step is then to set out the continuity conditions in order to obtain the relations between $\{r_G\}$ and $\{t_G\}$. So, at the interface of the two regions, i.e., at $z = 0$, we have:

- The continuity of the electric field, derived from $\hat{n}_{I,II} \times (\vec{E}_{II} - \vec{E}_I) = 0$, where $\hat{n}_{I,II}$ is the normal vector to the interface following the direction $I \to II$. This is,

$$|0\rangle + \sum_G r_G |G\rangle = \sum_G t_G |G\rangle , \tag{143}$$

  and if we project onto $|G\rangle$, we reach

$$r_G + \delta_{0,G} = t_G, \tag{144}$$

  where we have applied the basis vectors orthonormality.

- We must satisfy the boundary condition of the magnetic field: $\hat{u}_{I,II} \times (\vec{H}_{II} - \vec{H}_I) = \vec{j}(\alpha)$. This condition can be rewritten in the Dirac's notation as

$$|-\hat{u}_z \times \vec{H}_{II}(0)\rangle - |-\hat{u}_z \times \vec{H}_I(0)\rangle = -2\alpha |\vec{E}_{II}(0)\rangle , \tag{145}$$

  which is,

$$\sum_G Y_G^{II} t_G |G\rangle - Y_0^I |0\rangle + \sum_G Y_G^I r_G |G\rangle = -2\alpha \sum_G t_G |G\rangle . \tag{146}$$

  Now, projecting onto $|G\rangle$,

$$Y_G^{II} t_G - Y_0^I \delta G, 0 + Y_G^I r_G = -2\alpha t_G. \tag{147}$$

Therefore, combining Eqs. 144 and 147, we obtain that

$$r_0 = \frac{Y_0^I - Y_0^{II} - 2\alpha}{Y_0^I + Y_0^{II} + 2\alpha}, \tag{148}$$

and

$$t_0 = \frac{2Y_0^I}{Y_0^I + Y_0^{II} + 2\alpha}. \tag{149}$$

Also, $r_G = t_G = 0$, $\forall G \neq 0$. This means that the reflected and transmitted plane waves have the same momentum and polarization as the incident.

As a check, we will take a simple case and we will compare it with [29]. We consider normal incidence, i.e., $\vec{k}^0 = \vec{0}$, which implies that $Y^i_{\vec{0},p} = Y^i_{\vec{0},s} = \sqrt{\epsilon_i}$. We also consider that both regions are vacuum, in other words, $\epsilon_I = \epsilon_{II} = 1$. Introducing this constraints to the expressions for r_0 and t_0 we obtain that

$$r_0 = \frac{1 - 1 - 2\alpha}{1 + 1 + 2\alpha} = \frac{-\alpha}{1 + \alpha}, \tag{150}$$

and

$$t_0 = \frac{2}{1 + 1 + 2\alpha} = \frac{1}{1 + \alpha}, \tag{151}$$

which is exactly the same as [29] shows. Then, we can assume our reasoning has been well-made.

Now, we need to compute the energy flux of the incident, the reflected and the transmitted waves because the absorption is defined as

$$Abs_{2D} = (W_{inc} - W_{ref} - W_{tra})/W_{inc}. \tag{152}$$

In order to compute these EM energy fluxes we can have a look to App. C where we have already explained the pertinent procedure. We have to choose two planes where we will integrate the Poynting vector, these are $P_1 := (z = 0^-)$ and $P_2 := (z = 0^+)$. Hence,

$$\begin{aligned} W_{inc} &= \int_{P_1} d\vec{r}\, Re\left[\langle -\hat{u}_z \times \vec{H}_I^{inc}(\vec{r}, 0^-) | \vec{E}_I^{inc}(\vec{r}, 0^-)\rangle\right] \\ &= \int_{P_1} d\vec{r}\, Re\left[\left(Y_0^{I*}\langle 0|\right)\cdot\left(|0\rangle\right)\right] = Re\left[Y_0^{I*}\right] = Y_0^{I*}, \end{aligned} \tag{153}$$

$$\begin{aligned} W_{ref} &= \int_{P_1} d\vec{r}\, Re\left[\langle -\hat{u}_z \times \vec{H}_I^{ref}(\vec{r}, 0^-) | \vec{E}_I^{ref}(\vec{r}, 0^-)\rangle\right] \\ &= \int_{P_1} d\vec{r}\, Re\left[\left(\sum_G Y_G^{I*} r_G^* \langle G|\right)\cdot\left(\sum_G r_G |G\rangle\right)\right] \\ &= \int_{P_1} d\vec{r}\, Re\left[\left(Y_0^{I*} r_0^* \langle 0|\right)\cdot\left(r_0 |0\rangle\right)\right] \\ &= Re\left[Y_0^{I*}|r_0|^2\right] = Y_0^{I*}|r_0|^2, \end{aligned} \tag{154}$$

$$\begin{aligned} W_{tra} &= \int_{P_2} d\vec{r}\, Re\left[\langle -\hat{u}_z \times \vec{H}_{II}(\vec{r}, 0^+) | \vec{E}_{II}(\vec{r}, 0^+)\rangle\right] \\ &= \int_{P_2} d\vec{r}\, Re\left[\left(\sum_G Y_G^{II*} t_G^* \langle G|\right)\cdot\left(\sum_G t_G |G\rangle\right)\right] \\ &= \int_{P_2} d\vec{r}\, Re\left[\left(Y_0^{II*} t_0^* \langle 0|\right)\cdot\left(t_0 |0\rangle\right)\right] \\ &= Re\left[Y_0^{II*}|t_0|^2\right] = Y_0^{II*}|t_0|^2 \end{aligned} \tag{155}$$

where we have removed $Re[\,\cdot\,]$ because we will only consider propagating waves and thus Y_0^{i*} are real.

Therefore, the absorption of the 2D film is

$$Abs_{2D} = \frac{Y_0^{I*}(1 - |r_0(\alpha)|^2) - Y_0^{II*}|t_0(\alpha)|^2}{Y_0^{I*}}. \tag{156}$$